1
2
3

The prolactin receptor scaffolds Janus kinase 2 via co-structure formation with phosphoinositide-4,5-bisphosphate

6
7

Raul Araya-Secchi[1,2], Katrine Bugge[3#], Pernille Seiffert[3#], Amalie Petry[4], Gitte W. Haxholm[3], Kresten Lindorff-Larsen[3], Stine F. Pedersen[4*], Lise Arleth[1*] and Birthe B. Kragelund[3*],

[1]Structural Biophysics, Section for Neutron and X-ray Science, Niels Bohr Institute, University of Copenhagen, 2100 Copenhagen, Denmark.
[2]Facultad de Ingenieria Arquitectura y Diseño, Universidad San Sebastian, Bellavista 7, Santiago, Chile.
[3]Structural Biology and NMR Laboratory (SBiNLab), Department of Biology, University of Copenhagen, 2200 Copenhagen, Denmark.
[4]Section for Cell Biology and Physiology, Department of Biology, University of Copenhagen, 2200 Copenhagen N, Denmark

#contributed equally

*Corresponding author: bbk@bio.ku.dk.
Correspondence also to arleth@nbi.ku.dk and sfpedersen@bio.ku.dk

Running title: Co-structure formation by PRLR, JAK2 and PI(4,5)P$_2$

Abstract

Class 1 cytokine receptors transmit signals through the membrane by a single transmembrane helix to an intrinsically disordered cytoplasmic domain that lacks kinase activity. While specific binding to phosphoinositides has been reported for the prolactin receptor (PRLR), the role of lipids in PRLR signalling is unclear. Using an integrative approach combining NMR spectroscopy, cellular signalling experiments, computational modelling and simulation, we demonstrate co-structure formation of the disordered intracellular domain of the human PRLR, the membrane constituent phosphoinositide-4,5-bisphosphate (PI(4,5)P$_2$) and the FERM-SH2 domain of the Janus kinase 2 (JAK2). We find that the complex leads to accumulation of PI(4,5)P$_2$ at the transmembrane helix interface and that mutation of residues identified to interact specifically with PI(4,5)P$_2$ negatively affects PRLR-mediated activation of signal transducer and activator of transcription 5 (STAT5). Facilitated by co-structure formation, the membrane-proximal disordered region arranges into an extended structure. We suggest that the co-structure formed between PRLR, JAK2 and PI(4,5)P$_2$ locks the juxtamembrane disordered domain of the PRLR in an extended structure, enabling signal relay from the extracellular to the intracellular domain upon ligand binding. We find that the co-structure exists in different states which we speculate could be relevant for turning signalling on and off. Similar co-structures may be relevant for other non-receptor tyrosine kinases and their receptors.

Keywords: IDP, NMR, simulation, prolactin receptor, JAK2, single-pass transmembrane receptors, PI(4,5)P$_2$,

Introduction

56
57   Cytokine receptors are transmembrane glycoproteins that bind cytokines on the cell surface and
58   transduce signals across the membrane to the interior of the cell. This, in turn, activates signalling
59   pathways leading to multiple outcomes including induction of immune responses, cell proliferation,
60   altered metabolism and differentiation (Brooks et al., 2016). Class 1 cytokine receptors constitute a
61   subclass of receptors that transverse the membrane by a single α-helical transmembrane domain
62   (TMD) (Brooks et al., 2016), separating a folded extracellular domain (ECD) from a disordered
63   intracellular domain (ICD). The prolactin (PRL) receptor (PRLR) is one of the structurally most
64   simple cytokine receptors (*Figure 1*). Signaling by the PRLR/PRL complex is implicated in the
65   regulation of more than 300 biological functions in vertebrates (Bole-Feysot et al., 1998), and its
66   function is especially well-known for its essential role in mammary gland development and lactation
67   (Hannan et al., 2022). Apart from this, deregulation of PRLR/PRL signalling is associated with
68   several pathologies in humans of which hyperprolactinemia resulting in reproductive failure is best
69   described (Bachelot and Binart, 2007; Newey et al., 2013). Deregulation of PRLR/PRL signaling is
70   linked to other diseases and, although still debated, suggested to be implicated in the development
71   and progression of prostate (Sackmann-Sala and Goffin, 2015) and breast (Clevenger and Rui, 2022)
72   cancers.
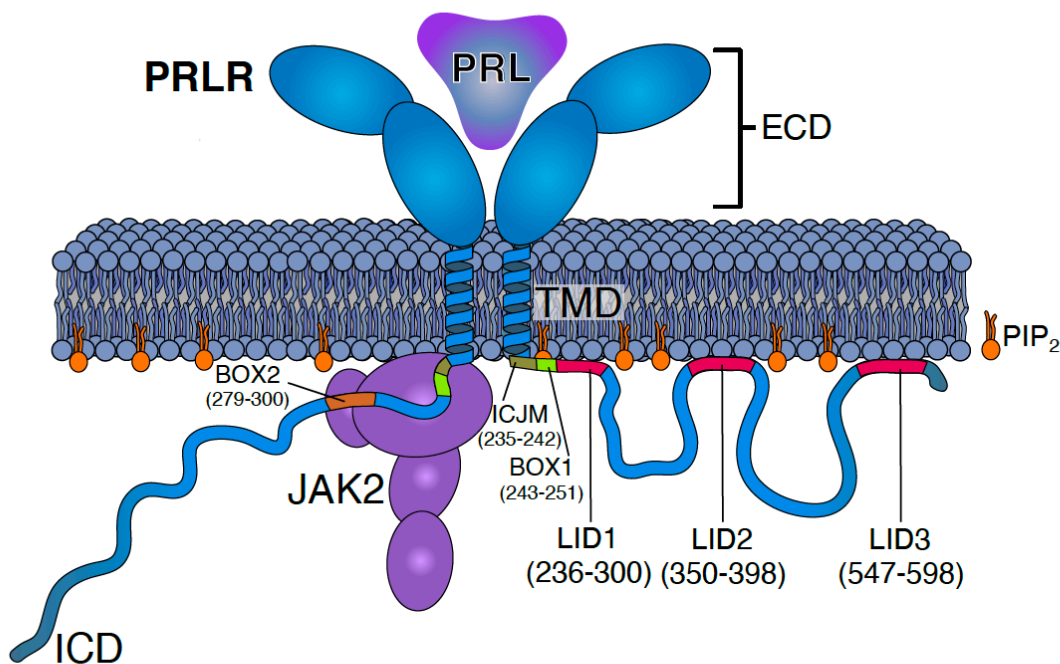
73
74
75   **Fig. 1: Schematics of the PRLR:PRL:JAK2 complex in the membrane.** The PRLR is shown in light blue, the PRL as
76   a dark blue triangle, the PRLR-ICD as a disordered chain and JAK2 in purple. The PI(4,5)P$_2$ lipid (PIP$_2$) is shown in
77   orange. The intracellular juxtamembrane (ICJM) region and BOX1 of PRLR-ICD are highlighted in green nuances, while
78   the three LIDs as defined in Haxholm et al., (Haxholm et al., 2015) are highlighted in red. For simplicity only one of the
79   two ICDs is shown associated with JAK2 via the BOX1 (green) and BOX2 (orange) motifs.

80
81   For cytokine receptors, signal transduction through the membrane is received by an ICD, which is
82   intrinsically disordered and lacks kinase activity (Haxholm et al., 2015). Thus, association of

3

83   auxiliary kinases is mandatory for signalling, with the Janus kinases (JAK1–3) and the tyrosine kinase
84   TYK2 being the most thoroughly described (Brooks et al., 2016; Morris et al., 2018). A proline-rich
85   region constituting the so-called BOX1 motif close to the membrane, as well as a second hydrophobic
86   motif termed BOX2, are known to be essential for JAK binding (**Figure 1**) (Ferrao et al., 2018;
87   Rowlinson et al., 2008). However, although progress has been made in the molecular understanding
88   of cytokine binding and despite several structures of folded ECDs (Broutin et al., 2010; de Vos et al.,
89   1992), TMDs (Bocharov et al., 2018; Bugge et al., 2016), a complete receptor (Kassem et al., 2021)
90   and a receptor ICD in complex with JAK1 (Glassman et al., 2022) have emerged, it is still not clear
91   how the signal inside the cell is received by the disordered region to elicit and in turn control signal
92   transduction.

93

94   A subset of class 1 cytokine receptors form homodimers and trimeric complexes with their ligands,
95   with the main dimerization occurring in the TMDs (Brooks et al., 2014; Brown et al., 2005; Gadd
96   and Clevenger, 2006; Kubatzky et al., 2001; Seubert et al., 2003). This group includes the growth
97   hormone receptor (GHR), the erythropoietin receptor (EPOR), the thrombopoietin receptor (TPOR)
98   and the PRLR, which have become well-established paradigmatic models. Recently, signal
99   transduction by the GHR has been suggested to occur via a rotation of the transmembrane helices
100   within the dimer leading to a subsequent separation of the ICDs (Brooks et al., 2014; Brown et al.,
101   2005). A torque is hereby exerted on the associated JAK2s, which is thought to relieve inhibition by
102   the pseudokinase domains, initiating signalling. The ICDs of these receptors have been shown to be
103   highly disordered (Haxholm et al., 2015), a feature which is preserved in models of the PRLR (Bugge
104   et al., 2016) and the full-length GHR in nanodiscs (Kassem et al., 2021). This brings forward the
105   question of how signalling is orchestrated by disorder and how a disordered linker region between
106   the TMD and the region bound to the kinases can communicate and transduce information.

107

108   For both the PRLR and the GHR, lipid interaction domains (LID) with affinity for negatively charged
109   lipids have been identified in their ICDs (Haxholm et al., 2015). Common to both receptors is that
110   they contain a LID proximal to the membrane, directly overlapping with the JAK2 interaction sites,
111   BOX1 and BOX2 (Seiffert et al., 2020). Using nuclear magnetic resonance (NMR) spectroscopy we
112   identified three LIDs in the PRLR-ICD termed LID1, LID2 and LID3 (**Figure 1**) (Haxholm et al.,
113   2015) and using lipid dot-blots we showed that the PRLR-ICD has variable affinities for different
114   membrane constituents, including for different phosphoinositides (PIs). In particular, PRLR has a
115   distinct affinity for phosphoinositide-4,5-bisphosphate ($PI(4,5)P_2$) and lacks affinity for $PI(3,4,5)P_2$
116   (Haxholm et al., 2015). PIs are important constituents of the membrane and play key roles in
117   signalling, both as membrane interaction partners that can be specifically modulated by
118   phosphorylation (Carracedo and Pandolfi, 2008), and as secondary messengers (McLaughlin et al.,
119   2002; Suh and Hille, 2005). Indeed, some single-pass receptors contain conserved anionic lipid
120   interaction sites close to the membrane (Hedger et al., 2015a) and increasing evidence suggest lipid
121   interaction to take on important regulatory roles (McLaughlin et al., 2005; Metcalf et al., 2010).
122   Recently, the epidermal growth factor receptor (EGFR) was shown to sequester $PI(4,5)P_2$ by
123   accumulating it around the TMD regulating the dimer/monomer equilibrium and with a possible
124   positive feedback loop through the activation of the phospholipase C (PLC) – diacylglycerol (DAG)-

4

125 IP$_3$ pathways (Maeda et al., 2018). This will lead to subsequent conversion of PI(4,5)P$_2$ to PI(3,4,5)P$_3$
126 and hence depletion of PI(4,5)P$_2$ from the membrane. Similar depletion of PI(4,5)P$_2$ from the plasma
127 membrane has been noted under hypoxia (Lu et al., 2022). For class 1 cytokine receptors the role of
128 PIs in signalling is less clear.

130 In a cellular context, signalling-related proteins can be membrane anchored through modifications
131 such as acylation (Patwardhan and Resh, 2010; Rawat et al., 2013; Rawat and Nagaraj, 2010) or via
132 designated lipid-binding domains. This includes the four point-1, ezrin, radixin moesin (FERM)
133 domain of radixin, focal adhesion kinase (FAK) and the protein tyrosine phosphatase L1 (PTPL1)
134 (Bompard et al., 2003; Feng and Mertz, 2015; Hamada et al., 2000), the SH2 domains of the Src
135 family kinases (Park et al., 2016; Sheng et al., 2016) and the FERM-SH2 domain of merlin (Mani et
136 al., 2011). Thus, kinases and receptors can co-localize at the plasma membrane without necessarily
137 being bound within a complex. It is, however, unclear whether such membrane co-localisation has
138 functional consequences, such as enhancing signalling speed, and whether the membrane may act as
139 an additional scaffolding platform that enhances binding via restriction in the two-dimensional plane.

141 Recent work on disorder in membrane proteins and on the interplay between membrane proteins and
142 lipids have revealed the need for strong integrative methods, combining successfully various
143 structural biology techniques, biophysics and computational biology (Basak et al., 2022; Larsen et
144 al., 2022). These include NMR, small-angle X-ray scattering, crosslinking-mass spectrometry and
145 single molecule fluorescence combined with molecular dynamics simulations (Chavent et al., 2018;
146 Goretzki et al., 2023). These efforts have provided important insights into the role of lipids in
147 regulation of membrane proteins. For TRPV4, a member of the TRP vanilloid channel family, it was
148 shown that an autoinhibitory patch of the receptor competed with PI(4,5)P$_2$ binding at the membrane
149 to attenuate channel activity, and MD simulation showed that lipid binding affected the ensemble
150 dynamics(Goretzki et al., 2023). For EphA2, a receptor tyrosine kinase, an integrative study showed
151 how PIs mediate the interaction between the kinase domains, facilitated by clustering of PIPs via
152 binding to the receptor juxtamembrane domain (Chavent et al., 2018) further promoting conformation
153 specific dimerization (Stefanski et al., 2021). Thus, studying dynamic processes at the membrane
154 interface is an emerging field requiring integrative structural biology approaches for detailed atomic
155 resolution information.

157 For the PRLR it is still not clear whether, and if so how, interactions between the ICD and the
158 membrane impact signal transduction and association with JAK2. Nor is it understood how structural
159 disorder can relay and transmit information from the TMD to initiate signalling. To shed light on the
160 molecular details underlying a potential interplay between the receptor, membrane and kinase we
161 focused on the human PRLR and its LID1 closest to the membrane, facilitating the first intracellular
162 step in signaling. Using an integrative approach combining NMR spectroscopy, cell biology and
163 computational modelling, we demonstrate the formation of a co-structure comprised of the disordered
164 PRLR-ICD, the membrane constituent PI(4,5)P$_2$ and the FERM-SH2 domain of the JAK2. Facilitated
165 by this co-structure, the disordered region closest to the membrane forms an extended structure, which

166 we suggest stabilizes the disordered domain, allowing signal relay from the extracellular to the
167 intracellular domain.
168
169 **Results**
170 **LID1 is disordered in solution and when tethered to the transmembrane helix**
171 Membrane interactions by PRLR-ICD have previously been studied in the absence of anchoring to
172 the TMD defining three LIDs, with LID1 closest to the membrane (Haxholm et al., 2015). Since
173 tethering would increase the local concentrations at the membrane and the ICD, this could affect
174 affinity, complex lifetime as well as the degree by which structure formation would be captured.
175 Furthermore, the first LID, LID1, is disordered and is located in the juxtamembrane region where it
176 is responsible for transmitting information on extracellular hormone binding to the bound JAK2. As
177 this constitutes the very first step on the intracellular side, and given the distance to the other two
178 LIDs (LID2 and LID3) and their disconnect from the TMD by long disordered regions, we focused
179 exclusively on LID1. We recombinantly expressed the TMD (residues 211–235 with numbering
180 corresponding to the processed protein) with five residues added at the two termini (TMD$_{F206-V240}$),
181 and the TMD with the first 35 residues of LID1, TMD-ICD$_{F206-S270}$ (*Figure 2A*). We then examined
182 their structural propensities in detergents and in small unilamellar vesicles (SUVs) by NMR
183 spectroscopy. In 1,2-dihexanoyl-sn-glycero-3-phosphocholine (DHPC) micelles, most of the TMD
184 resonances of the TMD$_{F206-V240}$ and TMD-ICD$_{F206-S270}$ variants were readily superimposable in the
185 ^{15}N,^{1}H-HSQC spectra (*Figure 2 - figure supplement 1*), suggesting that the conformation of the TMD
186 was not affected by the presence of the ICD. For the TMD-ICD$_{F206-S270}$, C$^{\alpha}$ NMR resonances were
187 collected for most of the disordered region, while backbone carbon resonances for the TMD, except
188 for A222, and the region G236-P246 immediately following it, were broadened beyond detection in
189 the 3D spectra, preventing assignments (*Figure 2B)*. This may suggest that the first ten residues of
190 the ICD interact with or are buried in the micelles, or are affected by the overall slower tumbling of
191 the micelle, whereas the complete overlap of the TMD residues in the ^{15}N-HSQC spectra confirm the
192 helical structure as seen previously. We assigned the backbone nuclei of the detectable resonances of
193 TMD-ICD$_{F206-S270}$ in DHPC micelles and compared the secondary chemical shifts (SCS) to those of
194 the ICD alone (ICD$_{G236-Q396}$) (*Figure 2C*). Whereas the region of the ICD that is undetected in TMD-
195 ICD$_{F206-S270}$ formed transient extended structures in the absence of the TMD, the observable parts
196 were highly similar suggesting lack of structure induction by TMD tethering or the micelles. In 1-
197 palmitoyl-2-oleoyl-sn-glycero-3-phosphocholine (POPC) SUVs, only the resonances of the most C-
198 terminal residues of TMD-ICD$_{F206-S270}$ were detectable; however, the chemical shifts suggested that
199 the residues were disordered (*Figure 2 – figure supplement 2*). Taken together, these results suggest
200 that most of the ICD residues remain disordered when tethered to the TMD and in the presence of a
201 neutral membrane mimetic.
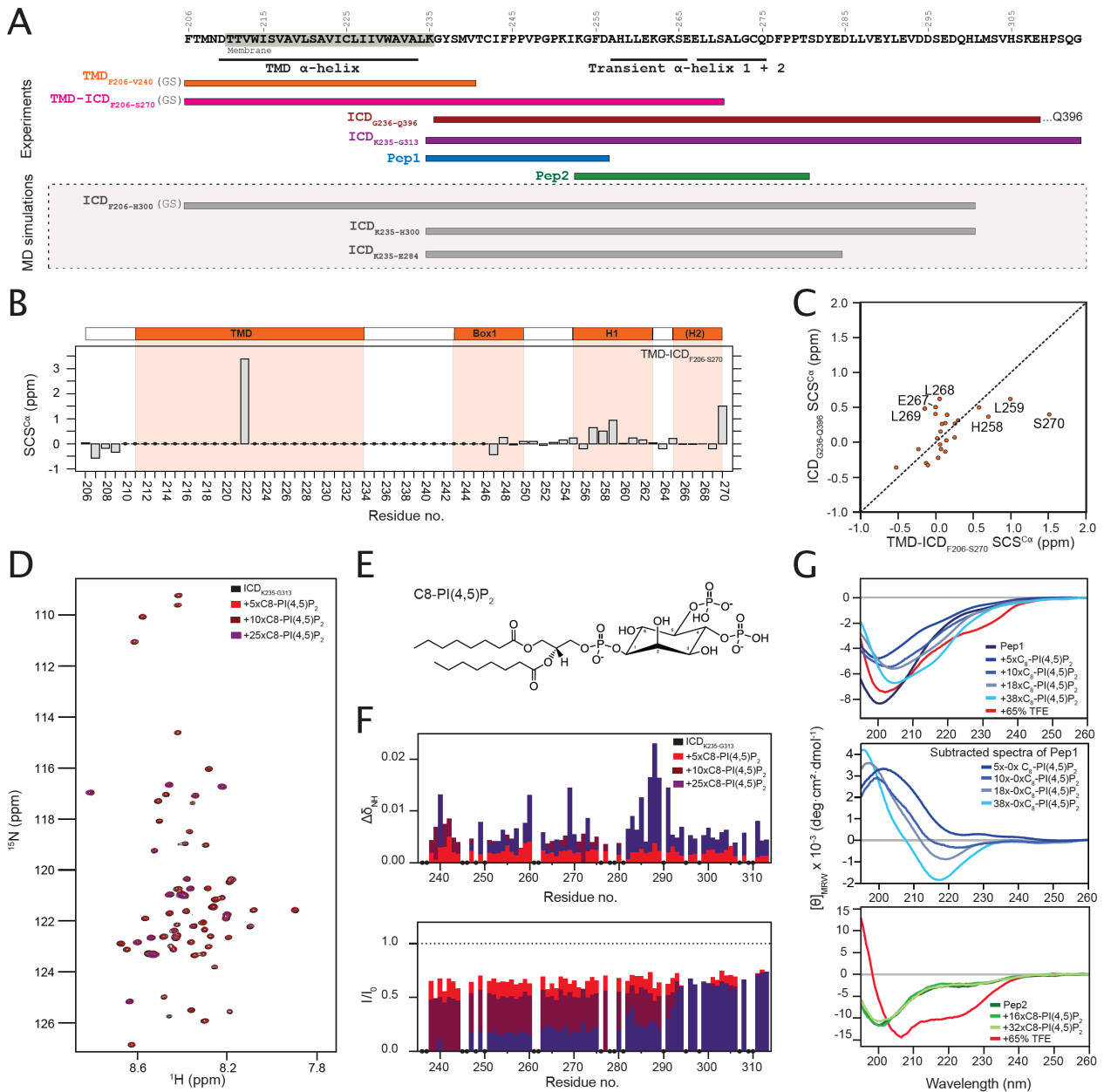
202
203
204 **Fig. 2: The ICJM region of the PRLR interacts with PI(4,5)P₂. A)** Overview of investigated PRLR variants. **B)**
205 Secondary chemical shifts (SCSs) of TMD-ICD$_{F206-S270}$ reconstituted in DHPC micelles. **C)** Correlation plot of the SCSs
206 of ICD$_{G236-Q396}$ plotted against those of TMD-ICD$_{F206-S270}$. **D)** ^{15}N,^{1}H-HSQC spectra of ^{15}N-ICD$_{K235-G313}$ titrated with 5x,
207 10x and 25x molar excess of C$_8$-PI(4,5)P$_2$. **E)** Structure of C$_8$-PI(4,5)P$_2$. **F)** Backbone amide chemical shift perturbations
208 (CSPs) and peak intensity changes upon addition of C$_8$-PI(4,5)P$_2$ to ^{15}N-ICD$_{K235-G313}$ plotted against residue number. **G)**
209 **Top**: Far-UV CD spectra of Pep1 titrated with C$_8$-PI(4,5)P$_2$ or in 65% TFE. **Middle:** Far-UV CD spectra of Pep1 in the
210 presence of 5x-38x C$_8$-PI(4,5)P$_2$ subtracted with the spectrum of Pep1 in the absence of C$_8$-PI(4,5)P$_2$. **Bottom**: Far-UV
211 CD spectra of Pep2 titrated with C$_8$-PI(4,5)P$_2$ or in 65% TFE. * indicate missing data points.
212 **Figure supplement 1**: ^{15}N, ^{1}H-HSQC spectra of A) TMD$_{F206-V240}$ and TMD-ICD$_{F206-S270}$ in DHPC micelles, and (B) TMD-
213 ICD$_{F206-S270}$ in POPC SUVs.
214 **Figure supplement 2**: C$^{\alpha}$ secondary chemical shifts of ICD$_{G236-Q396}$
215
216

7

LID1 binds PI(4,5)P$_2$ in the juxtamembrane region forming extended structures

217
218   PRLR-ICD has previously been shown to bind PI(4,5)P$_2$ (but not PI(3,4,5)P$_3$) (Haxholm et al., 2015),
219   suggesting that this lipid could modulate membrane affinity and the structural properties of the PRLR-
220   ICD. To separate headgroup effects from lipid bilayer surface effects, we used a short-chain C$_8$-
221   PI(4,5)P$_2$, which has a high critical micelle concentration (CMC) of 2 mM (Goñi et al., 2014) and
222   analysed the structural changes by NMR and CD spectroscopy at concentrations below the CMC
223   (Goñi et al., 2014) to identify the binding site.

224
225   ^{15}N-labelled ICD$_{K235-G313}$ covering LID1 (*Figure 1*) was titrated with C$_8$-PI(4,5)P$_2$ and binding was
226   assessed by ^{1}H-^{15}N-HSQC spectra (*Figure 2D-F*). The chemical shift perturbations (CSPs) were
227   modest whereas substantial intensity changes were observed throughout the chain, supporting a direct
228   interaction between the ICD and lipids. The resonances from G236-F244 completely disappeared
229   suggesting exchange on an intermediate NMR timescale, while intensities were substantially reduced
230   in the V247-S290 region (*Figure 2F*). In the region from D285-E292 we observed an almost inverse
231   correlation between the CSPs and the intensities. This suggests that in contrast to the preceding
232   region, a faster local exchange rate allows us to follow the resonances from the bound state in this
233   region, giving rise to the large CSPs. From this region and to the C-terminus, only moderate intensity
234   changes were observed (*Figure 2F*). These findings suggest that the primary PI(4,5)P$_2$ binding site
235   is located closest to the membrane in what we define as the intracellular juxtamembrane (ICJM)
236   region (K235-C242). The ICJM is located N-terminally to the BOX1 motif ($_{243}$IFPPVPGPK$_{251}$
237   (UNIPROT); $_{245}$PPVPGPK$_{251}$ (elm.eu.org)).

238
239   As the resonance-broadening precluded observation of the bound state, two overlapping peptides,
240   Pep1 (K235-D256) and Pep2 (K253-T280), were constructed and evaluated by CD spectroscopy. In
241   isolation, the peptides were disordered as judged by the negative ellipticity at 200 nm in their far-UV
242   CD spectra (*Figure 2G*). Pep1 and Pep2 were titrated with C$_8$-PI(4,5)P$_2$ and the structural changes
243   monitored (*Figure 2G*). For Pep2, the far-UV CD signal was unaffected by the presence of C$_8$-
244   PI(4,5)P$_2$. In contrast, for Pep1, large spectral changes were seen, which were unrelated to helix
245   formation. Subtracting the spectra in the presence and absence of C$_8$-PI(4,5)P$_2$, revealed a negative
246   ellipticity minimum at 218 nm, a strong indicator of β-strands, showing that when bound to C$_8$-
247   PI(4,5)P$_2$, a distinct extended (strand-like structure) signature was seen (*Figure 2G*). This suggests
248   that this region of LID1 changes its conformational properties upon binding to C$_8$-PI(4,5)P$_2$. We
249   evaluated the intrinsic helical propensies of the two ICD segments by exposure to high
250   trifluorethanol (TFE) concentrations. Here, Pep2 was readily able to form helical structure as
251   expected from the presence of two transient helices (Haxholm et al., 2015) (*Figure 2G, top*), whereas
252   Pep1 was not (*Figure 2G, bottom*).

253
254   In summary, LID1 of the PRLR-ICD interacts with PI(4,5)P$_2$, with the primary interaction site located
255   in the K235-S290 region. Headgroup interaction was dominantly located to the region K235-D256
256   constituting the ICJM and the BOX1 motif and this interaction induced the formation of a regional
257   extended structure in the PRLR-ICD.

258

LID1 has specific PI(4,5)P$_2$ contacts which drive PI(4,5)P$_2$ recruitment

To obtain a more detailed characterization of the behaviour of the disordered PRLR-ICD near lipid bilayers, as well as the effect of different anionic lipid headgroups in these, we turned to molecular simulations. Here, as explained above, we focused on the LID1 (K235-H300), alone and in context of TMD, and first placed a coarse-grained (CG) model of the TMD-ICD$_{F206-H300}$ in three different mixed-membrane systems. These contained an upper leaflet consisting of 100% POPC and lower leaflets composed of a 90:5:5 or 80:10:10 mixture of POPC:POPS:PI(4,5)P$_2$ (***Figure 3AB***) or a 70:30 molar ratio mixture of POPC:1-palmitoyl-2-oleoyl-sn-glycero-3-phospho-L-serine (POPS) (***Figure 3 – figure supplement 1EF***). Since the Martini forcefield may produce unrealistically collapsed disordered regions, increasing the strength of the protein-water interactions by 8–10% has provided satisfactory results when applied to the simulation of other disordered regions or multidomain proteins (Thomasen et al., 2022). Thus, the simulations were run using a modified version of the Martini3 forcefield with a 10% increase in the strength of the protein-water interactions. For comparison, similar simulations were performed using the Martini2 forcefield (***Figure 3 – figure supplement 1***).

We first analysed the dynamics of the LID1 during the simulations focusing on the pattern of protein-lipid contacts. Here, we measured the number of protein-lipid contacts focusing either on interactions between the protein and lipid headgroups or the protein and lipid acyl chains. In both cases we determined the fraction of the simulation time that the protein and different parts of the lipid were within 7Å of each other. In general, we observed that residues in the N-terminal part of the LID1 (K235 - D255), which includes the ICJM and BOX1, established contacts with the bilayer in all three membrane systems (***Figure 3A,B, Figure 3 – figure supplement 2***) Furthermore, a hydrophobic region rich in prolines (V240–P250) made consistent contacts with the acyl-chains and much more than to the headgroups, indicating penetration into the lower-leaflet. Similar behaviour has been reported with CG-MD simulations for the juxtamembrane region of other single-pass transmembrane receptors (Hedger et al., 2015b). For PRLR, the pattern of interaction was independent on the lipid composition, at least in terms of protein-POPC contacts, and the region interacting with the lipids was similar in all three membrane systems (***Figure 3A,B, Figure 3 – figure supplement 2***).

Although the extent and pattern of protein-lipid interactions appeared constant, a striking observation was made in both systems containing PI(4,5)P$_2$. Here, protein-lipid interactions between residues K235 and K253 and PI(4,5)P$_2$ were present during a large fraction (≥50%) of the simulations, despite PI(4,5)P$_2$ being present at only 5% or 10% of the total lipids (***Figures 3 – figure supplement 2***). This was also observed in simulations with the Martini2 forcefield, in which the LID1 promptly collapsed in a globular and unstructured coil (***Figure 3 – figure supplement 1***). This suggested that PI(4,5)P$_2$ spontaneously accumulated, or in other ways become concentrated around the TMD-ICD$_{F206-H300}$. The computed average density maps for PI(4,5)P$_2$ indeed showed that PI(4,5)P$_2$ formed a microdomain around the TMD (***Figure 3D***). The low frequency of contacts between the protein and POPS suggests that POPS did not accumulate or compete with PI(4,5)P$_2$ for binding to the TMD-ICD$_{F206-H300}$, further supporting the preference for PI(4,5)P$_2$ observed earlier (Haxholm et al., 2015).

9

300   Similar preference was also observed with 5% PI(4,5)P$_2$ (*Figure 3 – figure supplement 2*) as well as
301   with Martini2 (*Figure 3 – figure supplement 2E-F*).
302
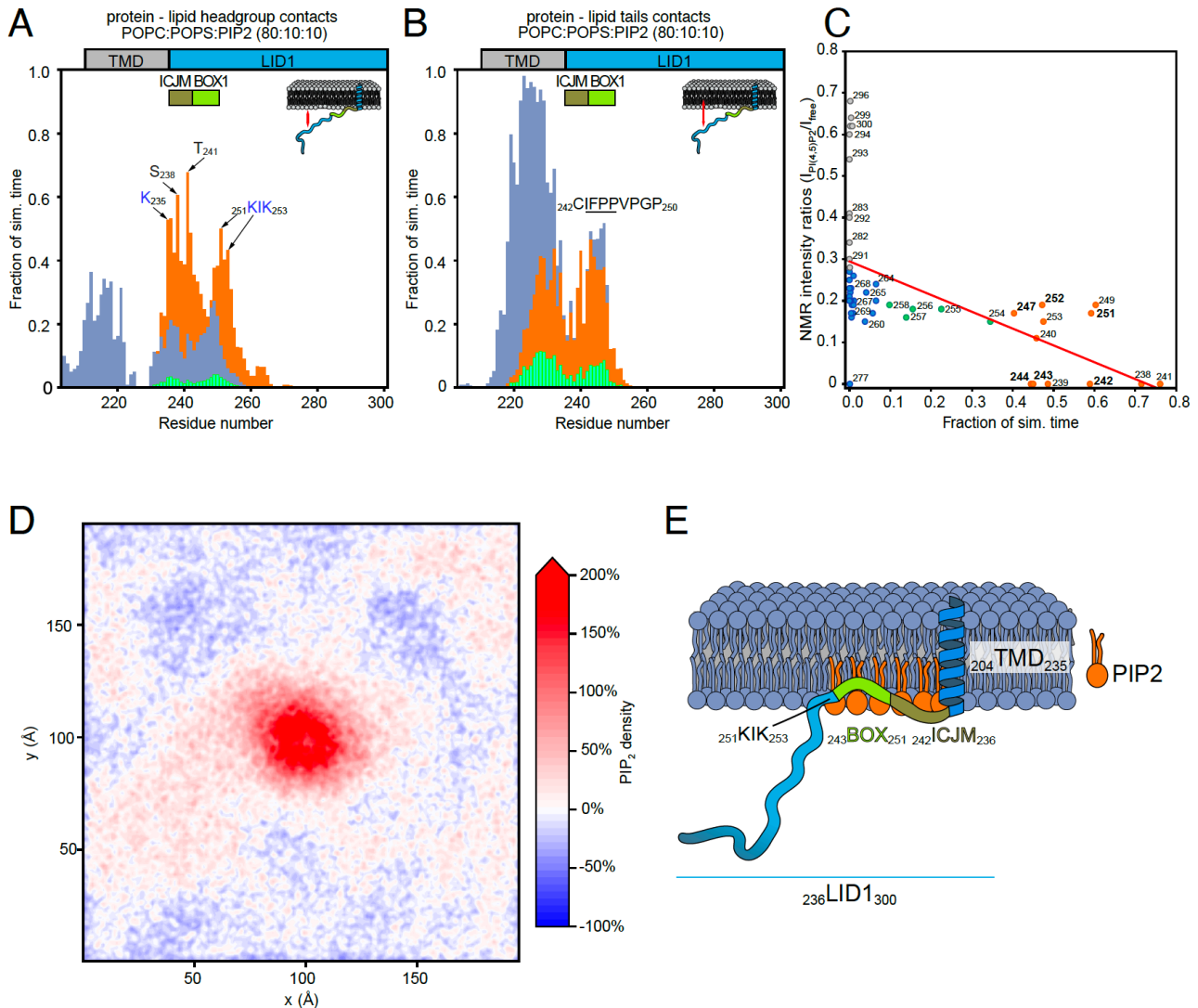
303
304
305   **Fig. 3. Protein – lipid interactions of PRLR-ICD$_{LID1}$ obtained from CG-MD simulations. (A-B)** Protein – lipid
306   contact histograms for PRLR-ICD$_{LID1}$ + POPC:POPS:PI(4,5)P$_2$ (80:10:10). **A)** Contacts between the protein and lipid
307   headgroups. A contact is counted if the distance between the backbone beads of the protein is ≤ 7 Å from the head-group
308   beads of the lipids. **B)** Contacts between the protein and the acyl chains of the lipids. A contact is counted if the distance
309   between the backbone bead of the protein is ≤ 7 Å from the acyl-chain bead of the lipids. **C)** Correlation between the
310   change in NMR signal and the contact frequency between PRLR-ICD$_{LID1}$ and the lipid headgroups from the PRLR-
311   ICD$_{LID1}$ + POPC:POPS:PI(4,5)P$_2$ (80:10:10) system. Pearson correlation coefficient of -0.55 with $p = 4.0\times10^{-5}$ and $R^2=$
312   0.3. **D)** Average PI(4,5)P$_2$ density map (xy-plane) taken from the PRLR-ICD$_{LID1}$ + POPC:POPS:PI(4,5)P$_2$ (80:10:10)
313   simulation. The map is colored according to the enrichment/depletion percentage with respect to the average density
314   value. **E)** Schematic representation of how the interactions and the embedment into the membrane of PRLR contribute to
315   the co-structure formation. The data from the simulations correspond to those of the production stage (see methods).
316
317   **Figure supplement 1**: *Protein – lipid interactions of PRLR-ICD$_{LID1}$ obtained from CG-MD simulations using the martini*
318   *3.0b3.2 forcefield*

10

319 **Figure supplement 2**: Complementary analysis of the Protein – lipid interactions of PRLR-ICD$_{LID1}$ obtained from CG-
320 MD simulations.

321

322 A more detailed analysis of LID1-PI(4,5)P$_2$ contacts revealed a preference for certain residues, shown
323 as peaks in the protein-headgroup contact profiles. In particular K235, S238, T241, and K251 and
324 K253, which define a KIK motif suggested as a PI(4,5)P$_2$ binding motif (Kjaergaard and Kragelund,
325 2017), engaged in highly populated contacts (***Figure 3A and figure supplement 2A***). The pattern of
326 contacts was not affected by PI(4,5)P$_2$ concentration; however, the frequency of contacts almost
327 doubled as a result of the increase from 5% to 10% of PI(4,5)P$_2$. The hydrophobic residues in the
328 ICJM and BOX1 penetrate the headgroup layer and facilitate the approximation of the KIK motif to
329 the PI(4,5)P$_2$ headgroups. The stabilization of the structure provided by the hydrophobic residues
330 from the ICJM and BOX1 is also reflected in their decrease in flexibility, observed as a shoulder on
331 the RMSF-BB plot, for the residues that comprise the ICJM and BOX1 of PRLR-LID1. Very similar
332 profiles of the RMSF-BB plot was obtained for the systems with respectively 5 and 10% PI(4,5)P$_2$ in
333 POPC:POPS, suggesting that the loss in flexibility is coupled to the buried hydrophobic residues
334 rather than to specific PI(4,5)P$_2$ interaction (***Figure 3 – figure supplement 2C).*** Contributions from
335 other positively charged residues such as K262 and K264 were very small. To validate the
336 observations from the simulations, we compared the pattern of protein:PI(4,5)P$_2$ interactions
337 observed in the NMR experiments to those from the simulations containing PI(4,5)P$_2$ (***Figure 3C***).
338 A clear correlation between loss of NMR signal and high frequency of protein-PI(4,5)P$_2$ and
339 POPC/POPS contacts in the 80:10:10 simulation was observed, reinforcing that the simulations are
340 able to capture the specificity of protein-PI(4,5)P$_2$ interactions. Furthermore, both experiments
341 (***Figure 2***) and simulations (***Figure 3***) show that the residues involved in binding to PI(4,5)P$_2$-
342 containing membranes overlap with those that are involved in binding to JAK2.

343

344 In summary, the CG-simulations of TMD-ICD$_{F206-H300}$ near lipid membranes showed accumulation
345 of PI(4,5)P$_2$ around the TMD and the N-terminus of LID1 involving the ICJM and BOX1. The
346 residues made contact with the membrane independently of lipid type, with BOX1 residues acting as
347 a tether by penetrating the headgroups. This tethering keeps positively charged residues, such as K251
348 and K253, near the membrane. This may be the driver for PI(4,5)P$_2$ recruitment, enhanced by higher
349 PI(4,5)P$_2$ concentration. Intriguingly, we observed that the same regions involved in JAK2 binding
350 (BOX1), also play roles in membrane association and lipid recruitment.

351

352 **JAK2-FERM-SH2 and PRLR-ICD$_{LID1}$ form co-structures with PI(4,5)P$_2$ on membranes**
353 It has been suggested that JAK2 and PRLR interact constitutively in cells (Campbell et al., 1994; Rui
354 et al., 1994) although recent data for the GHR have shown that the Src family kinase Lyn competes
355 for this site (Chhabra et al., 2023). Thus, given our observations that residues from LID1 form lipid-
356 specific contacts with the membrane constituents using the same region covering the binding interface
357 with the FERM domain of JAK2, we decided to explore the structure and dynamics of the
358 JAK2(FERM-SH2):PRLR(LID1) complex near lipid bilayers (***Figure 4***). To do so, an atomistic
359 model of the complex of a smaller region of PRLR-ICD$_{K235-E284}$ bound to the JAK2-FERM-SH2
360 domains (residues P37 to T514) was built, taking advantage of crystal structures of JAK2-FERM-

361 SH2 and of JAK1-FERM-SH2 and TYK2-FERM-SH2 bound to analogous fragments of the ICDs of
362 the interferon λ- and α-receptors (IFNLR1 and IFNAR1), respectively. This model was used to
363 perform all-atom MD simulations in a water-box to obtain equilibrated structures for further
364 simulations, and to study the dynamics of the protein complex. The average contact map between
365 JAK2-FERM-SH2$_{P37-T514}$ and PRLR-ICD$_{K235-E284}$ showed clusters of contacts in which residues from
366 BOX1 of LID1 formed close contacts (avg. dist. ≤ 4Å) with residues from the F2 lobe (and the F1-
367 F2 linker) and the SH2 domain of JAK2-FERM-SH2, respectively (***Figure 4 – figure supplement***
368 ***1A***). C-terminally to BOX1, a second set of persistent contacts was observed, again involving charged
369 and hydrophobic residues including F255, L259, E261, K262 and K264 from PRLR-ICD$_{K235-E284}$.
370 Conservation analysis using ConSurf (Ashkenazy et al., 2016; Landau et al., 2005) (***Figure 4 – figure***
371 ***supplement 1B-D***) showed conserved residues in the interface, particularly those of BOX1 of PRLR
372 (P245, P248, K251, I252) (***Figure 4 – figure supplement 1B),*** while a patch of conserved residues
373 (T225, I229 and F236) in JAK2-FERM-SH2 formed close contact with residues from PRLR BOX1.
374 JAK2 residues V183 and L184 interacted with the backbone of $_{251}$KIK$_{253}$ of PRLR-ICD, whereas
375 other, less conserved residues such as E173 and E177 formed transient salt-bridges with K251 and
376 K253 of PRLR-ICD (see ***Figure 4 – figure supplement 1A)***. The contact map also showed that the
377 N-terminus of the ICJM remained flexible without close contacts with JAK2-FERM-SH2 (avg. dist.
378 ≥ 6Å).
379
380 Next, an equilibrated structure of the JAK2-FERM-SH2:PRLR-ICD$_{K235-E284}$ complex was used to
381 build a coarse-grained model, which was then placed near lipid bilayers of different lower leaflet
382 composition. A number of randomly positioned starting orientations were placed ~7 Å below the
383 lower leaflet (16 orientations for the POPC:POPS:PI(4,5)P$_2$ (80:10:10) membrane and eight for the
384 POPC:POPS (70:30) membrane). In addition we included twelve orientations of JAK-FERM-SH2
385 without the PRLR-ICD$_{K235-E284}$ placed near a POPC:POPS:PI(4,5)P$_2$ (80:10:10) membrane. For the
386 JAK2-FERM-SH2:PRLR-ICD$_{K235-E284}$ complex near a 70:30 POPC:POPS membrane, binding to the
387 lower leaflet was observed for only three of the eight systems (***Figure 4 – figure supplement 2A***). In
388 contrast, when PI(4,5)P$_2$ was present (10%), rapid binding of the complex to the membrane was
389 observed in all simulations reaching 97% saturation (***Figure 4 – figure supplement 2A***). Both
390 proteins in the complex showed specific clusters of residues with contacts to PI(4,5)P$_2$, POPS and
391 POPC, independent of the initial orientations (***Figure 4BC***). The number of contacts formed was
392 higher for the simulations with PI(4,5)P$_2$. This suggests that contacts with other components of the
393 membrane occur close to the bound PI(4,5)P$_2$. Overall, the PRLR-ICD $_{K235-E284}$ showed a pattern of
394 lipid contacts similar to the simulations of PRLR TMD-ICD$_{G204-H300}$ with the POPC:POPS:PI(4,5)P$_2$
395 (80:10:10) membrane (***Figure 4C***), with residues K$_{235}$GY$_{237}$contacting PI(4,5)P$_2$ headgroups for at
396 least 50% of the total contact time and with insertion into the membrane; note that this occurs even
397 though PRLR-ICD$_{K235-E284}$ is not tethered to the membrane via the TMD. Also, like in the PRLR
398 TMD-ICD$_{G204-H300}$ simulations, contacts made by C242 and I243 to POPC were still present. In
399 contrast, contacts by other residues from BOX1 and the KIK motif has lower populations. However,
400 and as expected from the location of the most frequent PRLR-ICD $_{K235-E284}$/lipid contacts, JAK2-
401 FERM-SH2 had more contacts in the F2 lobe of the FERM domain, mainly involving residues I223,
402 L224, R226, K227 and R230, constituting the regions where the N-terminus of PRLR-ICD$_{K235-E284}$ is

12

403 bound (*Figure 4B*). In the JAK2-FERM-SH2 simulations without PRLR-ICD and near a
404 POPC:POPS:PI(4,5)P$_2$ (80:80:10) membrane, we observed that simulations initiated in eleven out of
405 the twelve orientations ended up binding to the membrane (*Figure 4 – figure supplement 2A*). In this
406 case, the overall binding pattern of protein-lipid contacts remained similar.
407
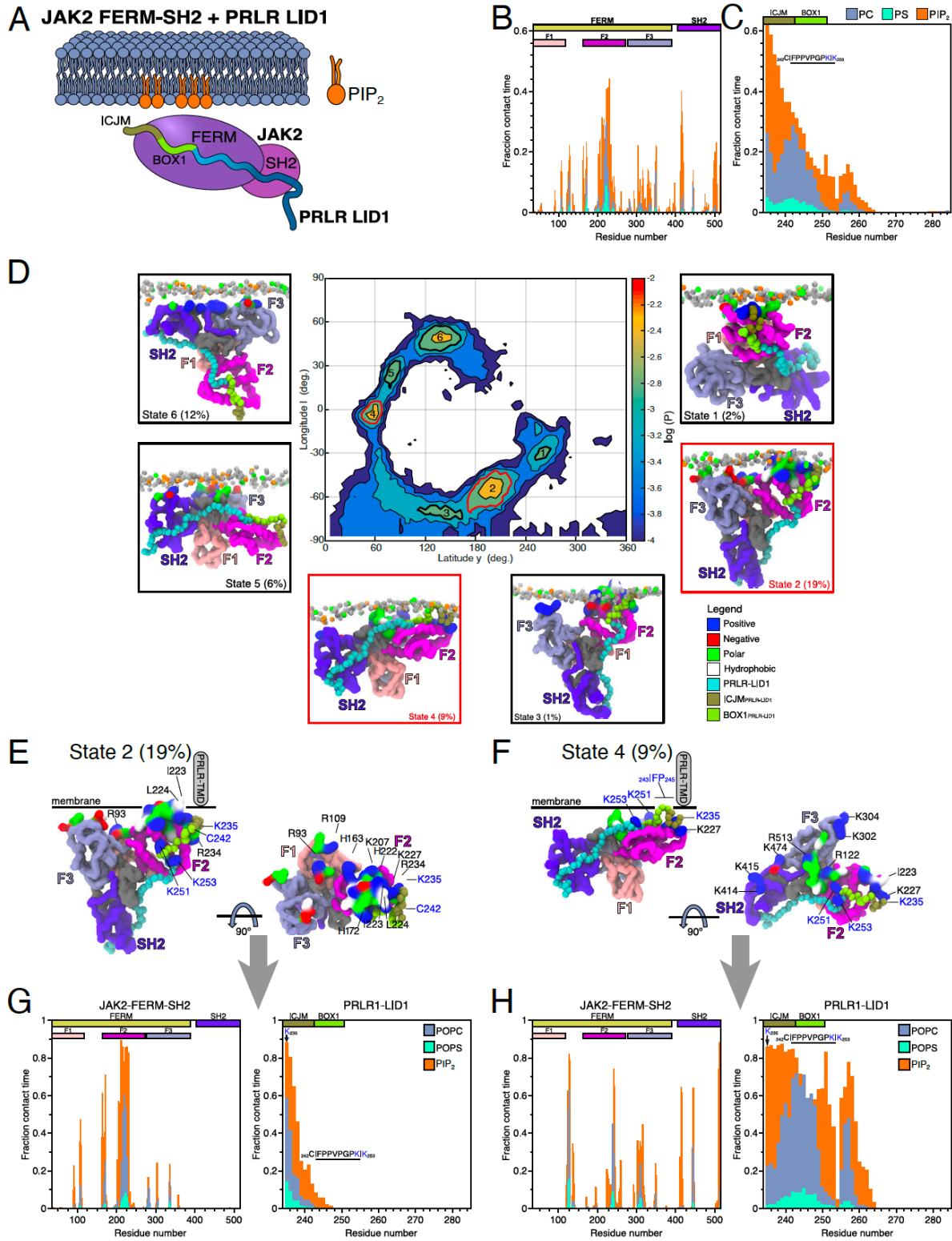
408

409 **Fig. 4. Protein – lipid interactions of the JAK2-FERM-SH2 PRLR-ICD$_{LID1}$ complex obtained from CG-MD**
410 **simulations**. **A)** Schematic representation of the simulated system. Combined **B)** JAK2-FERM-SH2-lipid and **C)** PRLR-
411 ICD$_{LID1}$-lipid contact frequency histograms for the 16 CG simulations of the JAK2-FERM-SH2 +PRLR-ICD$_{LID1}$+
412 POPC:POPS:PI(4,5)P$_2$ system. **D)** Distribution of the orientations adopted by the JAK2-FERM-SH2 + PRLR-ICD$_{LID1}$
413 complex when bound to lipids taken from the 16 simulations with POPC:POPS:PI(4,5)P$_2$ in the lower-leaflet. The
414 snapshots surrounding the map correspond to representative conformations of the highlighted states also indicating the
415 fraction total bound time for which each state was observed. Representative conformations of **E)** State 2 and **F)** State 4.
416 The grey cylinder depicts the position where PRLR-TMD should be located. Representative protein-lipid contact
417 histograms for **G)** State2 and **H)** State4 colored as in panels B and C.
418 **Figure supplement 1**: *Analysis of the JAK2-FERM-SH2- PRLR-ICD$_{LID1}$ AA-MD simulation*.
419 **Figure supplement 2.** *Complementary analysis of Protein – lipid interactions of the JAK2-FERM-SH2 PRLR-ICD$_{LID1}$*
420 *complex obtained from CG-MD simulations*
421 **Figure supplement 3.** *Snapshots of the different binding states observed for the JAK2-FERM-SH2 – PRLR-ICD$_{LID1}$*
422 *complex with the complete structural model of JAK2*
423
424 Previous studies have suggested that the Martini2 forcefield model underestimates cation-π
425 interactions between surface aromatic residues and choline headgroups on the membrane (Khan et
426 al., 2020). However, this may not be applicable to other types of protein-membrane interactions,
427 particularly where negatively charged headgroups are present. Our simulations involving PI(4,5)P$_2$
428 and POPS suggest that interactions between PRLR and the bilayer are primarily driven by positively
429 charged residues in the protein, and that other protein-membrane interactions are secondary or occur
430 between the lipids and residues that surround positively charged residues interacting with a PI(4,5)P$_2$
431 (or POPS) lipid. As a result, cation-π interactions may not be as important for the protein-lipid contact
432 patterns we observed, but could be one explanation as to why we observe less frequent binding in the
433 POPC:POPS systems.
434
435 In summary, our simulations showed that binding of JAK2 to the membrane was enhanced by the
436 presence of PI(4,5)P$_2$ and that the ICD from PRLR and JAK2 formed a co-structure with PI(4,5)P$_2$
437 maintaining the contacts to the lipids observed for the individual proteins. The presence of PI(4,5)P$_2$
438 was essential for the membrane interactions.
439
440 **The complex between JAK2-FERM-SH2 and LID1 shows preferential bound orientations with**
441 **membranes containing PI(4,5)P$_2$**
442 To characterize the membrane-bound modes of the complex in more detail, we took inspiration from
443 Vogel *et al.* (Herzog et al., 2017) and constructed a map that represents the populations of different
444 orientations of the JAK2-PRLR-ICD$_{K235-E284}$ complex relative to the membrane and extracted
445 conformations to represent the most populated orientations as classified into states (***Figure 4D***). For
446 the JAK2-PRLR-ICD$_{K235-E284}$ complex bound to the POPC:POPS:PI(4,5)P$_2$ (80:10:10) membrane,
447 States 1–4 (~31% of the total contact time) showed the complex in an orientation where the N-
448 terminus of PRLR-ICD$_{K235-E284}$ contacted and inserted into the bilayer similarly to what was observed
449 in the PRLR TMD-ICD$_{G204-H300}$ simulations near a POPC:POPS:PI(4,5)P$_2$ bilayer. Of these four
450 states, States 1, 2 and 3 had the F2 lobe of the JAK2-FERM domain and the ICJM region of PRLR-
451 ICD$_{K235-E284}$ in contact with the membrane, penetrating below the headgroups, and acting as a pivot
452 over which the protein-complex rotates, leaving the complex to hang as a "Y" from the membrane

14

453 (See *Figure 4DE* and *MOVIE1*). State 4 on the other hand, while retaining the main contact points,
454 assumed a "flat" orientation with larger sections of the F2 lobe and F1-F2 linker from JAK2-FERM
455 and the entire N-terminal half of PRLR-ICD$_{K235-E284}$ (residues K235-G263) making a substantial
456 number of contacts with the membrane (*Figure 4DF* and *MOVIE2*). To examine whether the
457 identified states are compatible with functional states of the full-length kinase, we superimposed
458 representative conformations of States 1 to 6 with that of the full-length JAK2 model obtained from
459 the AlphaFold Protein Structure Database (UNIPROT O60674) (Jumper et al., 2021; Varadi et al.,
460 2022). This procedure revealed that both the Y (States 1, 2 and 3), and Flat (State 4) states keep the
461 other domains of JAK2 oriented towards the cytoplasmic space (*Figure 4 – figure supplement 3AD*),
462 supporting that these states could be functionally relevant. Furthermore, in the context of JAK2
463 dimerization required for signalling (Ferrao et al., 2018), these states allow for the correct orientation
464 for kinase domain dimerization. The two remaining states (States 5 and 6) showed an inverted
465 orientation in which the main protein-lipid interactions were formed by residues from the F3 lobe of
466 FERM and the SH2 domain, bringing the F2 lobe and the ICJM region of the PRLR-ICD
467 unrealistically far away from the membrane and from the connecting end of the TMD. Thus, States 5
468 and 6 appear functionally irrelevant, as further demonstrated by the superposition of the full-length
469 AlphaFold model of JAK2 in which the kinase domains would clash with the bilayer (*Figure 4 –*
470 *figure supplement 3EF*).

471

472 **Different membrane co-structures have different exposures relevant to signalling**
473 We analysed the protein-lipid interactions formed by States 2 (Y) and 4 (Flat) in more detail, and
474 despite overall similar contact profiles, some key differences were observed (*Figure 4E–4H*). For
475 the Flat state, an increase in contacts was seen for residues K235 to L260 of PRLR-ICD$_{K235-E284}$ with
476 a pattern similar to the one observed in the PRLR-TMD-ICD$_{G204-H300}$ simulations with PI(4,5)P$_2$
477 present. Dominant PI(4,5)P$_2$ contacts were seen for K235–C242, followed by POPC contacts for
478 residues C242–P248, with a second PI(4,5)P$_2$ contact peak for K251 and a third around H257. For
479 the Y state, only residues K235–Y237 made substantial contacts with PI(4,5)P$_2$ and/or POPC, leaving
480 BOX1 and the KIK motif exposed to the solvent and making contacts with JAK2. For JAK2-FERM-
481 SH2, the main difference between the Y and Flat states was a large decrease in contacts to the F2
482 lobe in the Flat state accompanied by an increase in contacts in F3 and SH2. Residues in the F2 lobe
483 involved in homodimerization, orientation and activation, including L224, K227, R230 and R234
484 (Wilmes et al., 2020) were only accessible in the Y state, and not in the Flat state. Thus, we speculate
485 that the Y and Flat states may mimic functionally relevant conformations pertaining to active and
486 inactive states of the signalling complex. Mapping of residues that make contacts with the bilayer in
487 the two states to the conservation maps shows that several positively charged residues of JAK2-
488 FERM-SH2 are largely conserved. Particularly K207, R226, K227 and R228 in F2 with high
489 population contacts with PI(4,5)P$_2$ in the Y state are highly conserved. Similar conservation was seen
490 for the positively charged residues K235, K414, K415 and R513, that form contacts with PI(4,5)P$_2$ in
491 the Flat state.

492

493 Similar simulations were performed near a POPC:POPS 70:30 bilayer, which resulted in only one of
494 eight systems showing stable binding to the bilayer characterized by only one state (*Figure 4 – figure*

495   *supplement 2A,B*). Here, residues from the F2 lobe of JAK2 form contacts with POPS lipids in a
496   narrow peak containing residues Q219 to R230, while for PRLR-ICD $_{K235-E284}$, residues from the
497   ICJM (K235-C242) and the BOX1 region (C242-P248), make high frequency contacts with both
498   POPS and POPC (*Figure 4 – figure supplement 2DE*). Overall this state is somewhat similar to State
499   3 observed for the simulations with PI(4,5)P$_2$. Similarly, for our simulations of JAK2-FERM-SH2
500   without PRLR near a bilayer with PI(4,5)P$_2$, 11 out of 12 stable binding conformations revealed three
501   most populated states (E1, E2, E3) (*Figure 4 – figure supplement 2C*). Characterization of these in
502   terms of protein-lipid contact profiles revealed that the positively charged residues in the F2 lobe play
503   an important role in binding to PI(4,5)P$_2$ in a similar manner as observed for the Y and Flat states of
504   the complex (*Figure 4 – figure supplement 2F*). Indeed, States 2 and 3 (*Figure4 – figure supplement
505   2GH*) show remarkable similarities with the Flat and Y state from the simulations of the JAK2-
506   FERM-SH2:PRLR-ICD$_{K235-E284}$ complex near a similar bilayer.
507
508   Overall, the simulations highlight preferential binding of both JAK2-FERM-SH2, both alone and in
509   complex with PRLR-ICD$_{K235-E284}$ to PI(4,5)P$_2$, and show that the absence of this lipid decreases the
510   level of LID1 binding to the bilayer. Even in the absence of TMD tethering, the most populated bound
511   states recapitulate the binding mode observed for the PRLR-ICD alone. Another key observation is
512   the existence of different states in which different regions of both JAK2 FERM-SH2 domain and
513   LID1 of PRLR are exposed to the solvent or hidden below the bilayer.
514
515   **Key residues for membrane interaction control cellular signalling efficiency**
516   From the NMR experiments and MD simulations we identified residues in LID1 that interact with
517   different components of the membrane and/or the FERM-SH2 domain of JAK2. This resulted in four
518   clusters positioned in the ICJM (K235-C242), the BOX1 region (C242–P248), two basic patches of
519   the KxK motif type (K251–K253 and K262–K264) and hydrophobic residues in the region
520   connecting them, respectively. To decipher the specific role of these clusters for PI(4,5)P$_2$ interaction,
521   we introduced four sets of mutations in ICD$_{K235-G313}$ and investigated the effect on PI(4,5)P$_2$
522   interaction using NMR spectroscopy. Based on the NMR data and simulations, we focused on the
523   KxK motifs, which would be involved in binding to PI(4,5)P$_2$ (*Figure 3A*) and JAK2 (*Figure 4 –
524   sumplement figure 1*), the CIF sequence, indicated to be important to membrane binding (*Figures 2
525   and 3B*) and four hydrophobic residues, where at least two were seen to be important for JAK2
526   binding (*Figure 4- supplement figure 1*). We avoided interfering directly with the BOX1 core motif
527   (P245–P250) (Pezet et al., 1997). Thus, the CIF motif (C242–F244) was mutated to GAG (GAG
528   mutant: C242G, I243A, F244G), while the lysines in the KxK motifs (251–253 and 262–264) were
529   all mutated to either glycines (K4G mutant: K251G, K253G, K262G, K264G) or, for charge reversal,
530   to glutamates (K4E mutant: K251E, K253E, K262E, K264E). Finally, four hydrophobic residues
531   (I$_{252}$, F$_{255}$, L$_{259}$ and L$_{260}$) were mutated to glycines (φ4G mutant). ^{15}N-PRLR-ICD$_{K235-G313}$ and the four
532   variants were titrated with up to 25× molar excess of C$_8$-PI(4,5)P$_2$, keeping the concentration below
533   the CMC. ^{1}H-^{15}N-HSQC spectra were recorded at each titration point and the changes in chemical
534   shifts and signal intensities were quantified (*Figure 5A*). Similarly to WT, all variants showed
535   negligible chemical shift changes (*Figure 5 – figure supplement 1*) but large peak intensity changes.
536   Decreased peak intensities were observed for all variants in the region of G236-D295, where the

537   changes were largest for the φ4G mutant and K4G, and similar to WT, while smaller effects were
538   seen for the GAG and the K4E variants, suggesting weaker affinities. Together, this indicates that the
539   KxK motifs and the CIF-motif are involved in $PI(4,5)P_2$ interaction, as expected from the contacts
540   predicted from simulation and NMR and CD data, yet none of these residues are essential for binding.
541
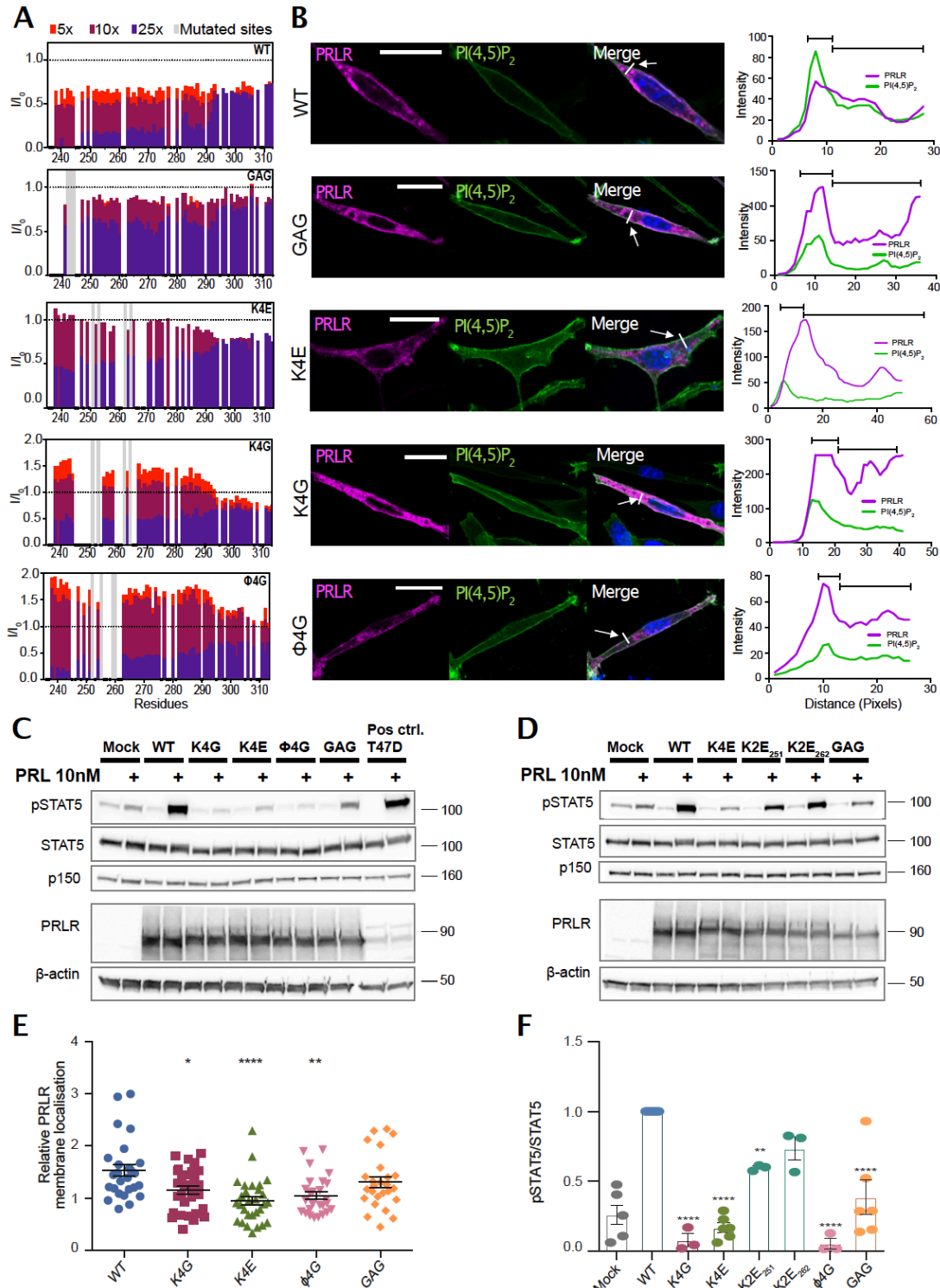
542

Fig. 5. PRLR variants with mutations in lipid interacting residues exhibit decreased PRL-stimulated STAT5 activation in AP1-2PH-PLCδ-GFP cells. A) NMR intensity changes of $ICD_{K235-G313}$ WT, K4G, K4E, φ4G and GAG variants upon titration with 5x, 10x and 25x molar excess C_8-PI(4,5)P_2 plotted against residue number. **B)** The PRLR variants (WT, K4G, K4E, φ4G, GAG) were transiently transfected in AP1 cells stably expressing the 2PH-PLCδ-GFP construct which visualizes the plasma membrane by binding PI(4,5)P_2. The cells were subsequently analysed by immunofluorescence microscopy, using antibodies against PRLR (magenta) and GFP (green), as well as DAPI (blue) to mark nuclei. To the right, examples of an average line-scan for each PRLR variant is shown. The fluorescence intensity depicted along the white line drawn (arrow) and green fluorescence (plasma membrane) was used to divide the line in a plasma membrane section and intracellular section, and relative membrane localization was calculated as the average fluorescence of PRLR in the membrane section divided by that in the intracellular section. **C, D)** AP1-2PH-PLCδ-GFP cells were transiently transfected with PRLR variants (WT, K4G, K4E, φ4G, GAG, $K2E_{253}$, $K2E_{261}$) and incubated overnight followed by serum starvation for 16-17 h and were subsequently incubated with or without 10 nM prolactin for 30 min. The resulting lysates were analysed by western blot for STAT5, pSTAT5 (Y964), PRLR, β-actin and p150 levels. The immunoblots are representative of three biological replicates. **E)** Ratio of plasma membrane localized receptor compared to intracellular receptor, analysed by line-scans as in B. Each point represents an individual cell, and data are based on three independent biological experiments per condition. Graphs show means with SEM error bars. *$P<0.05$, **$P<0.01$ and ****$P<0.0001$. One-way ANOVA compared to WT, unpaired. **F)** Quantification of western blot results shown as pSTAT5 normalized to total STAT5, relative to the WT condition. Graphs show means with SEM error bars. *$P<0.05$ and **$P<0.01$. One-way ANOVA compared to WT, unpaired.

Source file 1: Raw western blots (relating to *figure 5C*)
Source file 2: Raw western blot (relating to *figure 5D*)
Source file 3: Data summaries (relating to *figure 5E,F*)
Figure supplement 1: *Chemical shift perturbations of $ICD_{K235-G313}$ of A) WT, B) K4E, C) GAG, D) K4G and E) φ4G variants.*
Figure supplement 2: *^{15}N R_2 relaxation rates of $ICD_{K235-G313}$ of WT (grey bars), K4G (blue dots) and φ4G (red squares) variants.*

We observed dramatic increases in peak intensities for the K4G and φ4G variants in the presence of 5× and 10× molar excess of C_8-PI(4,5)P_2 when compared to WT (***Figure 5A***), suggesting changes in the dynamics of the chain. To adress this, we probed the backbone dynamics by acquiring ^{15}N R_2 relaxation rates of the WT, K4G and φ4G variants in the absence of C_8-PI(4,5)P_2 (***Figure 5 – figure supplement 2***). Compared to the WT, no major changes in R_2 were observed for two variants. The intensity increase observed for the K4G and φ4G variants during the titration with C_8-PI(4,5)P_2 therefore indicates increased backbone dynamics upon binding to C_8-PI(4,5)P_2 compared to the WT. Although we cannot explain this observation, it suggests that binding to C_8-PI(4,5)P_2 increases the dynamics of the first parts of the chain and thus require higher concentration of C_8-PI(4,5)P_2 to fully form the complex, as expected by the lower apparent affinity.

To address the implications of PI(4,5)P_2 interaction for PRLR membrane localization and downstream signalling, and to enable a potential separation of effect of perturbed membrane localization from direct PI(4,5)P_2 binding, we introduced the same four sets of mutations into the full-length PRLR. Together with WT PRLR, these were transiently transfected into AP1 mammalian epithelial cells, which were stably transfected with the fluorescent PI(4,5)P_2 reporter 2PH-PLCδ-GFP. The cells were subjected to fluorescence microscopy analysis of PRLR and the PI(4,5)P_2 reporter (Fig. 5B) and to western blot analysis of STAT5-activating phosphorylation (***Figures 5C-D, F-G***). None of the mutations fully abolished PRLR membrane localization. Western blot analysis

589 showed that the protein expression levels were similar for WT PRLR and all PRLR variants (***Figure***
590 ***5C***). However, compared to WT, the K4G, K4E and φ4G variants exhibited a significant reduction
591 in membrane localization as determined by line scan analysis (***Figures 5B,E***). This is in accordance
592 with their predicted JAK2 contacts obtained from the simulations, as JAK2 is known to be important
593 for PRLR trafficking (Huang et al., 2001). The PRL-induced STAT5 activation was significantly
594 decreased in cells expressing either the K4G, K4E or the φ4G variants, whereas STAT5 activation in
595 cells expressing the GAG variant was not significantly different from that of WT expressing cells
596 (***Figures 5C,F***). Decomposing the K4E variant into two individual mutants, in which only one of the
597 two KxK motifs was changed (K2E$_{251}$ and K2E$_{262}$) showed that the reduction in STAT5 activation
598 was attenuated in the variants with the individual mutations, compared to the drastic decrease
599 observed for the K4E mutant (***Figure 5D,G***). Thus, both KxK motifs are important for JAK/STAT
600 activation, which suggests that both PI(4,5)P$_2$ and JAK2 binding are important in this regard.

601

602 Taken together, these results show that while our data are consistent with the decreased membrane
603 localization contributing to the reduction of STAT5 activation, it is unlikely to account fully for the
604 effect observed for the K4G, K4E or the φ4G variants. Part of this reflects impaired binding to JAK2,
605 known to affect the amount of receptor at the cellular membrane. The MD simulations indicated that
606 only the first KxK motif is involved in lipid interaction while the second KxK motif is involved in
607 JAK2 interaction. Thus, a part of the the reduction in JAK/STAT activation in these variants could
608 arise from a combined effect of abolishing both PI(4,5)P$_2$- and JAK2 interaction within the LID1
609 region, which support the suggestion that co-structure formation between JAK2, PRLR and the
610 membrane is critical for optimal JAK/STAT signalling. However, within this co-structure, the
611 involved residues will likely affect several binding events, and thus separation of function by selective
612 mutations may not be straightforward.

613

614 **Discussion**
615 The sequence of the human PRLR has been known for more than 35 years (Boutin et al., 1988). Little
616 attention has, however, been given to the role of membrane composition for PRLR signalling, despite
617 it being placed in the plasma membrane where phosphoinositide levels are highly dynamic and
618 spatially variable, and being linked to cancer with lipid deregulation (Dadhich and Kapoor, 2022).
619 Here we asked if JAK2 and PRLR-ICD share a PI(4,5)P$_2$ binding site and if and how the binding to
620 PI(4,5)P$_2$ plays a role in the orientation of these proteins with respect to the membrane. Integrating
621 MD simulations with biophysical and cellular experiments has been critical in this endeavor. Our first
622 goal was to identify the residues of LID1 involved, as well as the structure formed—if any—in the
623 protein–lipid complex. Our results suggest that the residues that form the ICJM and BOX1 regions
624 of the ICD interact with the lipids via non-specific hydrophobic interactions that involve penetration
625 of the bilayer below the headgroups. This in turn enables positively charged residues of the $_{251}$KIK$_{253}$
626 motif to establish ionic interactions with PI(4,5)P$_2$ and in doing so the region folds into an extended
627 structure, similar to structures of other cytokine receptors in complex with either JAK1 or TYK2
628 (Wallweber et al., 2014; Zhang et al., 2016). In turn, PI(4,5)P$_2$ lipids accumulate around the TMD
629 and LID1 of PRLR, suggesting a relevant functional role of the interaction.

630

631 The results highlight the capacity of the LID1 to establish highly populated and specific interactions
632 with PI(4,5)P$_2$ via residues essential for its interaction with JAK2. Therefore, we addressed whether
633 LID1 in complex with the FERM-SH2 domain of JAK2 could engage with the lipid bilayer in the
634 absence of the TMD and with or without PI(4,5)P$_2$ lipids. Indeed, PI(4,5)P$_2$ was required for binding
635 of the complex to the membrane, as the presence of only POPS in the lower leaflet was not enough
636 to sustain binding despite its negative charge. Remarkably, when PI(4,5)P$_2$ was present, we observed
637 specific binding orientations that positioned the ICJM region of the LID1 in the same position as
638 when tethered to the TMD. Furthermore, in the complex, the protein-lipid contact profiles were
639 similar to the one observed for LID1 alone suggesting the PI(4,5)P$_2$ binding pattern to be maintained
640 in complex with JAK2. A detailed study of two of the most populated PRLR-bound states of JAK2
641 revealed a striking difference in orientation and contact pattern with the lipids, that could shed light
642 on functionally relevant states. For example, the most populated state, the Y state, had contacts from
643 the F2 lobe of the JAK2-FERM-SH2 domain and the ICJM of the PRLR, which penetrated the
644 membrane forming hydrophobic interactions with the acyl chains. In this orientation, regions of both
645 JAK2 and the PRLR that have been associated with receptor dimerization and activation for signaling
646 (Ferrao et al., 2018; Wilmes et al., 2020) are exposed to solvent and available for interactions. We
647 note that this orientation has resemblance to that shown in recent cryoEM structures of JAK1 bound
648 to IFNAR1 (Glassman et al., 2022). For the Flat state, we observed a drastic change in the protein-
649 lipid contact profiles for both proteins, but more markedly for LID1. While the main interaction site
650 remains the F2 lobe of JAK2 and the ICJM of the PRLR, the N-terminal residues of the LID1 now
651 lie sandwiched between the membrane and JAK2-FERM-SH2 domain and recapitulates the binding
652 pattern observed from TMD-ICD$_{F206-H300}$ simulations with membranes containing PI(4,5)P$_2$.
653 Remarkably, in this Flat state, most of the accessible regions in the Y states are now hidden under the
654 membrane. Thus, we speculate that the Y and Flat states may mimic an available and hidden state,
655 respectively, that could be relevant for regulation of dimerization and activation of signaling.
656 Interestingly, one residue that has been suggested to play a major role in JAK2 membrane association,
657 orientation, dimerization, and activation is L224 (Wilmes et al., 2020). This residue anchors into the
658 membrane only in the Y-state, and not in the Flat-state. Similarly, in simulations where L224 was
659 mutated to glutamate, a change in preferred orientation together with loss of dimerization and JAK2
660 and STAT5 phosphorylation was observed (Wilmes et al., 2020). This further highlight that the
661 orientation of the PRLR-JAK2 complex relative to the membrane has functional relevance.
662 Importantly, the presence of PI(4,5)P$_2$ in the membrane structurally tightens the path from the ECD,
663 folding the ICJM and BOX1 in an extended structure, making transmission of information of
664 hormone binding possible. Thus, signal relay by disordered linker of the PRLR can now be possible
665 through its complex formation with the membrane and JAK2 (*Figure 6*).

20
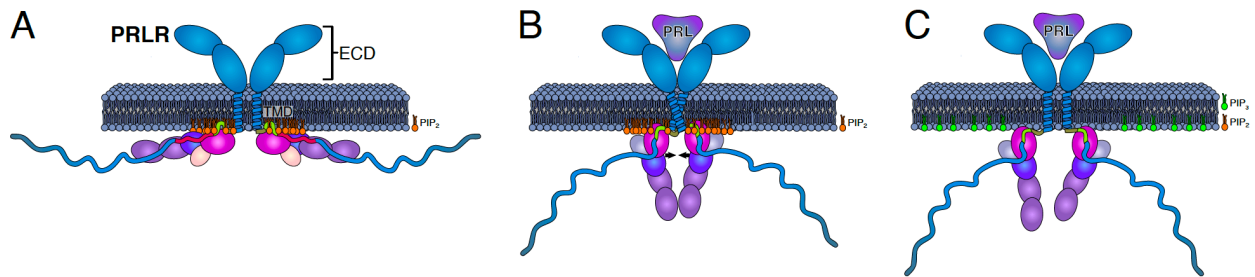
667
668 **Fig. 6. Model of how co-structure formation between JAK2, PRLR and PI4(4,5)P$_2$ may contribute to signalling**
669 **fidelity.** The suggested states in signalling would be **A**) the inactive state of the co-structure exemplified by the Flat
670 orientation. **B**) The hormone bound state exemplified by the co-structure in the Y orientation. **C**) Phosphorylation of
671 PIP(4,5)P$_2$ to PI(3,4,5)P$_3$ for which the PRLR has no affinity may lead to downregulation and/or termination of signalling.
672 The colour scheme of the proteins is identical to Fig.4.

673
674 Lastly, we tested the functional relevance of our observations by mutating residues that appeared
675 significant for PI(4,5)P$_2$:PRLR:JAK2 co-structure formation and determining their impact on cellular
676 PRL signaling. Both KxK motifs and the hydrophobic residues connecting them were important for
677 PI(4,5)P$_2$ interaction, PRLR membrane localization and cellular JAK2/STAT5 signaling. From the
678 MD simulation it was however evident that not all residues in these motifs were in direct contact with
679 the membrane, further highlighting that co-structure formation between PRLR, JAK2 and the
680 membrane is essential for optimal signal transduction. Another interesting observation was that even
681 though mutating the CIF motif had the largest impact on PI(4,5)P$_2$ binding, it had only a limited effect
682 on cellular JAK2/STAT5 signaling. Since the NMR results suggested that the ICJM serves as a
683 primary PI(4,5)P$_2$ anchoring point facilitating additional contacts along the chain, this could indicate
684 that a cooperative interaction within the co-structure is needed to control signaling and that PI(4,5)P$_2$
685 interaction is necessary for proper and substantial co-structure formation.

686
687 The PI(4,5)P$_2$-specific interactions observed point toward a possible regulatory role of PI(4,5)P$_2$ in
688 PRLR signaling. Our simulations showed that the membrane embedded TMD-ICD$_{F206-H300}$ was
689 associated with an accumulation of PI(4,5)P$_2$ around the TMD. One of the suggested roles of
690 PI(4,5)P$_2$ as a regulatory lipid is indeed to form microdomains around proteins and reduce their lateral
691 movement (Trimble and Grinstein, 2015; van den Bogaart et al., 2011). Another possible role can be
692 inferred from previous studies on the EGFR. Evidence suggests a positive feedback loop where
693 inhibition is released upon activation, because PI(4,5)P$_2$ is hydrolyzed to DAG and IP$_3$ by PLC$_y$
694 (Maeda et al., 2018; McLaughlin et al., 2005). Specifically, we have previously shown that PRLR
695 does not interact with PI(3,4,5)P$_3$ (Haxholm et al., 2015). As PI(4,5)P$_2$ is phosphorylated by the PI3-
696 kinase to PI(3,4,5)P$_3$ during PRLR signaling (Aksamitiene et al., 2011; Yamauchi et al., 1998), this
697 could indicate a way of attenuating signaling. Whether hydrolysis of PI(4,5)P$_2$ by PLC$_y$ is relevant
698 for PRLR signaling is not known.

699
700 **Conclusions**
701 Signal transduction by single-pass receptors through the membrane is still an enigma. In the present
702 work we identify co-structure formation of the disordered LID1 of the PRLR, the membrane

21

703 constituent PI(4,5)P$_2$ and the FERM-SH2 domain of the JAK2, and demonstrate its importance for

704 PRLR signalling. This co-structure has at least two orientations, a Y-shaped state extending from the

705 membrane and a Flat-state with sites hidden in the membrane, the functional roles of which await

706 further elucidation. The co-structure led to accumulation of PI(4,5)P$_2$ at the TMD interface and

707 mutation of residues identified to specifically interact with PI(4,5)P$_2$ negatively affected PRL-

708 induced STAT5 activation. Facilitated by the co-structure, the disordered ICJM folds into an extended

709 structure, tightening the path from the ECD to the ICD. We suggest that the co-structure formed

710 between receptor, kinase and PI(4,5)P$_2$ is critical for signal relay from the extracellular to the

711 intracellular side of the membrane, and that different orientations of the co-structure exist that may

712 represent inactive and active states.

713

714 **Materials and Methods**

715 **Expression and purification of TMD $_{F206-V240}$, TMD-ICD $_{F206-S270}$ and ICD$_{G236-Q396}$**

716 PRLR-ICD$_{G236-Q396}$ was produced as described in (Haxholm et al., 2015), and TMD$_{F206-V240}$ and

717 TMD-ICD$_{F206-S270}$ were produced as described in (Bugge et al., 2015).

718

719 **Expression and purification of ICD$_{K235-G313}$ and variants (K4E, K4G, ϕ4G and GAG)**

720 ICD$_{K235-G313}$ and variants hereof, K4E (K251E, K253E, K262E, K264E), K4G (K251G, K253G,

721 K262G, K264G), ϕ4G (I252G; F255G, L259G, L260G) and GAG (C242G, I243A, F244G) were all

722 produced as follows: Competent BL21(DE3) were transformed using heat shock transformation with

723 pET24a+ plasmids encoding the protein of interest with N-terminal His$_6$-SUMO tag. One colony

724 was used to inoculate 10 mL of LB media with 50 μg/mL Kanamycin and incubated overnight at 37

725 °C at 160 RPM. The overnight culture was used to inoculate 1L M9 minimal media (3 g/l KH$_2$PO$_4$,

726 7.5 g/l Na$_2$HPO$_4$, 5 g/l NaCl, 1 mM MgSO$_4$, 4 g/l glucose, 1 g ^{15}NH$_4$Cl$_2$, 1ml M2 trace solution, 50

727 μg/mL Kanamycin) and grown at 37 °C. At OD600 ~0.6 recombinant protein expression was induced

728 with 0.1 mM IPTG for 4H at 37 °C. Cells were harvested by centrifugation (5000xg, 20 min, 4°C)

729 and kept at -20 °C until purification. Cells were resuspended in 35 mL Buffer A (10 mM imidazole,

730 50 mM Tris (pH 8), 150 mM NaCl, 2 mM dithiothreitol (DTT) and lysed with French press at 25

731 kpsi, followed by centrifugation at 20.000xg, 45 min, 4 °C. The supernatant was applied to 5 mL of

732 pre-equilibrated Ni-NTA beads and incubated for 15 min followed by 50 mL wash with Buffer B 10

733 mM Imidazole, 50 mM Tris (pH 8), 1M NaCl, 2mM DTT) and 50 mL wash with Buffer A. Protein

734 was eluted with 10 mL Buffer C (250 mM Imidazole, 50 mM Tris (pH 8), 150 mM NaCl, 2 mM

735 DTT). The elution was supplemented with 0.01 mg ULP-1 and dialysed against 1 L of dialysis buffer

736 (50 mM Tris (pH 8), 150 mM NaCl, 1 mM DTT) overnight at 4 °C. The sample was re-applied to the

737 Ni-NTA column and incubated for 15 min. Flow through containing cleaved protein was collected,

738 and the remaining protein was eluted with 10 mL Buffer C. The sample was supplemented with 10

739 mM DTT before heating at 75 °C for 5 min with gentle rotation of the sample throughout. Sample

740 was transferred directly to ice for 10-15 min incubation followed by centrifugation at 20.000xg, 10

741 min, 4 °C. The supernatant was concentrated and supplemented with 5 mM betamercaptoenthaonl

742 (b-ME) before application to a HiLoad 16/60 Superdex75 prep grade column equilibrated in 20 mM

743   Na$_2$HPO$_4$/NaH$_2$PO$_4$, 150 mM NaCl, 5 mM b-ME (pH 7.3). Fractions containing pure protein were

744   pooled and concentrated

745

CD spectroscopy

747   The peptides covering residues K235-D256 (Pep1) and K253-T280 (Pep2), respectively were

748   purchased from KJ Ross (DK) at 95% purity from HPLC purification. The peptides were dissolved

749   in 10 mM Na$_2$HPO4/Na$_2$HPO4, pH 7.3 to a final concentration of 40 μM (Pep1) and 25 μM (Pep2)

750   and titrated with TFE or C$_8$-PI(4,5)P$_2$. The spectra were recorded in a 1mm Quartz cuvette on a Jasco-

751   810 spectropolarimeter purged with 8 l/min N$_2$ at 25 °C. A total of 10 accumulations were acquired

752   from 260-190 nm with the following settings: 0.5 nm data pitch, 1 nm band width, response time of

753   2 seconds, scanning speed of 10 nm/min. A background reference was recorded at identical settings

754   for each sample and subtracted from the relevant spectrum. The spectra were processed by fast

755   Fourier transform filtering and ellipticity converted to mean residual ellipticity ($[\theta]_{MRW}$)

756

NMR spectroscopy

758   *TMD$_{F206-V240}$ and TMD-ICD$_{F206-S270}$*

759   ^{15}N-labelled or ^{13}C,^{15}N-labeled TMD-ICD$_{F206-S270}$ was solubilized in molar excess 1,2-dihexanoyl-

760   sn-glycero-3-phosphocholine (DHPC) dissolved in 50 mM NaCl, 20 mM Na$_2$HPO$_4$/NaH$_2$PO4 buffer,

761   pH 7.2. Subsequently, the DHPC embedded TMD-ICD$_{F206-S270}$ was subjected to thorough buffer

762   exchange in a 3 kDa cutoff spinfilter to remove residuals. For reconstitution into POPC SUVs, ^{15}N-

763   labeled TMD-ICD$_{F206-S270}$ was solubilized in 300 μL 5:1 methanol:chloroform and mixed with molar

764   excess POPC dissolved in chloroform. The constituents were mixed, followed by evaporation of the

765   organic solvent under a stream of N$_2$. When the lipid film appeared dry, it was either left under a

766   stream of N$_2$ or placed under vacuum for at least an hour. The resulting proteoliposome film was

767   rehydrated with 1 mL of 50 mM NaCl, 20 mM Na$_2$HPO$_4$/NaH$_2$PO$_4$ buffer, pH 7.2, followed by

768   extensive dialysis against the buffer in a 3.5 kDa MWCO dialysis tube at 4 °C. Subsequently, the

769   proteoliposome solution was sonicated in an ultrasonication bath or, if the solution did not clarify,

770   with an UP400S Ultrasonic Processor, in rounds of 2 s with 30 s rest between runs. Finally, the sample

771   was concentrated in a 3 kDa cutoff spinfilter.

772   All NMR samples of ^{15}N-labelled or ^{13}C,^{15}N-labelled TMD-ICD$_{F206-S270}$ were added 10% (v/v)

773   D$_2$O, 2 mM tris(2-carboxyethyl)phosphine (TCEP), 1 mM sodium trimethylsilylpropanesulfonate

774   (DSS), 0.05% (v/v) NaN$_3$, and 50 mM NaCl, 20 mM Na$_2$HPO$_4$/NaH$_2$PO4 buffer (pH 7.2) to a final

775   volume of 370 μL followed by pH-adjustment to 7.2 (if needed). All spectra were acquired at 37 °C

776   because the peak intensities of the TMD region decreased at lower temperatures. Free induction

777   decays were transformed and visualized in NMRPipe (F Delaglio et al., 1995) and analysed using the

778   CcpNmr Analysis software (Vranken et al., 2005). Proton chemical shifts were referenced internally

779   to DSS at 0.00 ppm, with heteronuclei referenced by relative gyromagnetic ratios. For assignments

780   of backbone nuclei, heteronuclear NMR spectra of a sample containing 0.5 mM ^{13}C,^{15}N-labelled

781   TMD-ICD$_{F206-S270}$ in 500 times molar excess DHPC were acquired on a Bruker 750-MHz (^{1}H)

782   equipped with a cryoprobe. HNCACB and CBCA(CO)NH spectra were acquired with 32 and 40 of

783   transients, respectively, and 20% non-uniform sampling (Mayzel et al., 2014), and used for manual

784   backbone assignments. SCSs were calculated using random coil chemical shifts from (Kjaergaard et

785 al., 2011) (obtained by supplying primary structure, pH and temperature to the webtool
786 http://www1.bio.ku.dk/english/research/bms/research/sbinlab/groups/mak/randomcoil/script/),
787 which were subtracted from the assigned TMD-ICD$_{F206-S270}$ chemical shifts.
788 The ^{1}H,^{15}N-HSQC spectrum of 0.4 mM ^{15}N-labelled TMD-ICD$_{F206-S270}$ in POPC SUVs (100 times
789 molar excess of POPC) was acquired on a Varian INOVA 750- MHz (^{1}H) spectrometer equipped
790 with a room temperature probe. The number of transients was 104.
791
792 *ICD$_{K235-G313}$*
793 ICD$_{K235-G313}$ and the four variants (K4E, K4G, phi4G and GAG) were dialyzed at 4 °C overnight
794 against 20 mM Na$_2$HPO$_4$/NaH$_2$PO$_4$ (pH 7.3), 150 mM NaCl. The samples of 50 μM protein were
795 added 1 mM TCEP, 0.25 mM DSS and 10% (v/v) D$_2$O and centrifuged at 20.000 xg, 4 °C for 10 min
796 and transferred to 5mm Shigemi BMS-3 tubes. All NMR experiments were recorded at 5 °C on a
797 Bruker Avance III 600 MHz (^{1}H) spectrometer equipped with cryogenic probe. Free induction decays
798 were transformed and processed in qMDD (Orekhov and Jaravine, 2011), phased in NMRDraw
799 (Frank Delaglio et al., 1995) and analysed in CcpNMR analysis software (Vranken et al., 2005).
800 Proton chemical shifts were referenced to DSS and nitrogen and carbon to their relative gyromagnetic
801 ratios. ^{1}H-^{15}N-HSQC experiments were acquired using non-uniform sampling (Mayzel et al., 2014)
802 and recorded on 50 μM ^{15}N-ICD$_{K235-G313}$ (or variants) in the absence and presence of 5x, 10x and 25x
803 molar excess of C$_8$-PI(4,5)P$_2$ (Avanti Lipids 850185).
804 Transverse ^{15}N relaxation rates (R_2) of ICD$_{K235-G313}$ and the two variants, K4G and φ4G, were
805 acquired on Bruker Avance III 600 MHz (^{1}H) spectrometer with varying relaxation delays of 0 ms,
806 33.92 ms, 67.84 ms, 135.68 ms, 169.6 ms, 203.52 ms, 271.36 ms and 339,2 ms, measured in triplicates
807 and peak intensities fitted to single-exponential decays.
808
809 **Cell lines and media**
810 AP1-2PH-PLCδ-GFP cells (From J. Snipper; vector from Addgene plasmid #35142) were grown in
811 Minimum Essential Medium Eagle (EMEM, Gibco) containing 10% Fetal Bovine Serum (Sigma
812 Aldrich), 1% penicillin/streptomycin (Sigma), and 1% L-glutamine (Sigma). Stable AP1 clones
813 expressing 2PH-PLCδ-GFP were grown in the same medium, containing 600 μg/mL geneticin
814 (Merck-Millipore) to maintain expression of 2PH-PLCδ-GFP. Cell lines were maintained at 37 °C
815 with 95% humidity and 5% CO$_2$ and were passaged by gentle trypsination for a maximum of 15
816 passages.
817
818 **Immunoblotting**
819 Cells were grown to ~80% confluence in 6-well plates, washed in ice-cold PBS, lysed in boiling lysis
820 buffer (1% SDS, 10 mM Tris–HCl, pH 7.5, with phosphatase inhibitors), boiled for 1 min, sonicated,
821 and centrifuged to clear debris. Identical amounts of protein (12 μg/well) diluted in NuPAGE LDS
822 sample buffer (Novex) with 50% 0.5M DTT were boiled for 5 min, separated on Bio-Rad 10% Tris-
823 Glycine gels, and transferred to nitrocellulose membranes using the Trans-Blot Turbo Transfer
824 system (Bio-Rad). Membranes were stained with Ponceau S to confirm equal loading, blocked for 1
825 h at 37 °C in blocking buffer (TBST, 5% nonfat dry milk), and incubated with the relevant primary
826 antibodies in blocking buffer overnight at 4°C. After washing in TBST (TBS + 0.1% Tween-20),

827   membranes were incubated with HRP-conjugated secondary antibodies (1:2000, Sigma), washed in
828   TBST, and visualized using ECL reagent (Bio-Rad). Protein bands were quantified by densitometry
829   using ImageJ software, and normalized to those of STAT5 and then to WT.

830

831   **Immunofluorescence analysis**
832   For immunofluorescence experiments, cells were grown on 12 mm round glass coverslips to ~80%
833   confluency and fixed in 2% PFA (30 min at RT). Coverslips were washed three times for 3 x 5 min
834   in PBS, permeabilized for 15 min (0.5% Triton X-100 in TBS), blocked for 30 min (5% BSA in
835   TBST), and incubated with primary antibody in TBST + 1% BSA at RT for 1.5 h. Coverslips were
836   again washed in TBST + 1% BSA, and incubated with AlexaFluor488 and AlexaFluor568 conjugated
837   secondary antibody (1:600 in TBS + 1% BSA) for 1.5 h. Finally, coverslips were incubated with
838   DAPI (1:1000) for 5 min to stain nuclei, washed in TBST, and mounted in N-propyl-gallate mounting
839   medium (2% w/v in PBS/glycerol). Cells were visualized using the Olympus IX83 microscope with
840   a Yokogawa spinning disc confocal unit, using a 60X/1.4 NA oil emersion objective. Image
841   adjustments were carried out using ImageJ software. Line scans were performed using the
842   ColorProfiler ImageJ software plugin.

843

844   **Primary antibodies**
845   PRLR (Santa Cruz #SC20992), STAT5 (Santa Cruz #SC835), pSTAT5 (Y964) (Cell Signaling
846   #CS4322), p150 (BD #BD610473), β-actin (Sigma Aldrich #A5441).

847

848   **Modelling of simulated proteins**
849   *PRLR TMD-LID1 on a lipid bilayer*
850   To build a model of the hPRLR-TMD-ICD-LID1region (G204 to H300) we used the MODELLER
851   interface of Chimera (Pettersen et al., 2004; Webb and Sali, 2016). The structure of hPRLR-TMD
852   (PDB 2N7I (Bugge et al., 2016a)) was used as template for the transmembrane helix (in this structure
853   the residue at position 204 (P) was mutated to a G thus, in our model position 204 corresponds to a
854   glycine) and due to the lack of structural templates for the ICD, it was modelled as a disordered coil.
855   This all-atom model was used to build coarse-grained simulation systems where the TMD was
856   embedded in different lipid bilayers composed of POPC in the upper leaflet and either: i) POPC:POPS
857   (70:30), ii) POPC:POPS:PI(4,5)P_2 (90:5:5) and iii) POPC:POPS:PI(4,5)P_2 (80:10:10) in the lower
858   leaflet using the CHARMM-GUI martini_maker module (Jo et al., 2008; Qi et al., 2015). The
859   resulting systems were built using the Martini 2.2 forcefield topology and were later adapted to the
860   Martini 3 (version m3.b3.2) (Souza and Marrink, 2020) topology using the martinize2.py tool. For
861   these systems, the PI(4,5)P_2 parameters were adapted from their Martini2.2 version by changing the
862   names of the beads to the Martini3 naming scheme using as example other available lipids. These
863   Martini3 PI(4,5)P_2 parameters are available in our github repository (see the Data Avaliability
864   section). Secondary structure restraints from the Martini forcefield were only applied to the TMD and
865   no harmonic bond restraints were defined in the building of these systems.

866

867   *All-atom models of JAK2-FERM-SH2 and its complex with PRLR-ICD$_{LID1}$*

25

868 To build the JAK2-FERM-SH2 + PRLR-ICD$_{K235-E284}$ complex the following structures where used:
869 JAK1-FERM-SH2 + IFNLR1 (PDB 5L04 (Zhang et al., 2016)), TYK2-FERM-SH2 + IFNAR1 (PDB
870 4PO6 (Wallweber et al., 2014)) and JAK2-FERM-SH2 (PDB 4Z32 (McNally et al., 2016)). A
871 structural alignment of the three FEMR-SH2 domains was performed with STAMP (Russell and
872 Barton, 1992) using the Multiseq module (Roberts et al., 2006) of VMD (Humphrey et al., 1996).
873 The model of PRLR-ICD$_{K235-E284}$ was generated with the MODELLER interface of Chimera using as
874 template the aligned receptor-ICD regions present on the structures 5L04 and 4PO6. A total 200
875 models were generated, and the best in terms of its DOPE score (Shen and Sali, 2006) was selected
876 for further use. This resulted in a model of PRLR-ICD$_{K235-E284}$ bound to JAK2-FEMR-SH2. By
877 combining this model with chain A of PDB 4Z32, a structural model of the JAK2-FERM-SH2 +
878 PRLR-ICD$_{K235-E284}$ complex was obtained. All-atom simulation systems were built for JAK2-FERM-
879 SH2 and the JAK2-FERM-SH2+PRLR-ICD$_{K235-E284}$ complex model. The missing residues on the
880 loop of F3 of JAK2-FERM-SH2 were completed using CHARMM-GUI pbd-reader module (Jo et
881 al., 2014, 2008). Hydrogen atoms were automatically added to the protein using the psfgen plugin of
882 VMD (Humphrey et al., 1996). Aspartate, glutamate, lysine, and arginine residues were charged, and
883 histidine residues were neutral. Simulation boxes comprised of solvent and 150 mM NaCl were
884 generated using the CHARMM-GUI solution-builder module (Jo et al., 2008; Lee et al., 2016) using
885 CHARMM36m (Huang et al., 2017) parameters and topologies for the protein and the TIP3P water
886 model for the solvent.

887

888 *Coarsed-grained models of JAK2-FERM-SH2 and its complex with PRLR-ICD$_{LID1}$*
889 To build coarse-grained models of JAK2-FERM-SH2 and complex between JAK2-FERM-SH2 and
890 PRLR-ICD$_{K235-E284}$ complex, a conformation from their respective all-atom MD simulations of the
891 complex was taken after 150 ns (see below). These conformations were used to generate a CG model
892 using the martinize.py script. The Martini 2.2 forcefield (de Jong et al., 2013) was used and
893 intramolecular elastic bonds were defined for JAK2-FERM-SH2 in both systems. To keep the
894 complex formed and to avoid a "collapse" of the disordered PRLR-ICD$_{LID1}$, inter-molecular harmonic
895 bonds were also defined between JAK-FERM-SH2 and PRLR-ICD$_{K235-E284}$ in the complex. In both
896 cases, a force constant of 400 kJ mol^{-1} nm^{-2} and lower and upper elastic bond cut-offs of 5Å and 9Å,
897 respectively were used.

898

899 *Coarse-grained models of JAK2-FERM-SH2 and JAK2-FERM-SH2 + PRLR-ICD$_{LID1}$ near a lipid*
900 *bilayer*
901 The relaxed CG-model of the JAK2-FERM-SH2 + PRLR-ICD$_{LID1}$ complex or JAK2-FERM-SH2
902 alone (see below) was placed near (~ 7Å) pre-equilibrated lipid bilayers with wo different
903 compositions: POPC on the upper leaflet and two differen compositions on the lower leaflet: i)
904 POPC:POPS (70:30), and ii) POPC:POPS:PI(4,5)P$_2$ (80:10:10). The systems were solvated with
905 water beads and 150 mM NaCl. A total of 16 initial orientations of the protein were generated by
906 rotating the protein around the x or the y axis (with z being the normal of the membrane).

907

908 **Molecular dynamics (MD) simulations**
909 *Coarse-grained MD simulations*

26

910 Coarse-grained MD simulations were performed with Gromacs 2016 or 2018 using the Martini 2.2
911 force field (de Jong et al., 2013) or the open beta version of the Martini 3 (3.b3.2) force field (Souza
912 and Marrink, 2020). For the PRLR-TMD-ICD$_{K235-L284}$ simulations we increased the strength of
913 interactions between protein and water by 10% to avoid excessive compaction of the disordered
914 regions, as has been previously done for IDPs and multi-domain proteins (Kassem et al., 2021; Larsen
915 et al., 2020; Thomasen et al., 2022). Other simulation parameters, common to all the CG simulations
916 performed, were chosen following the recommendations in (de Jong et al., 2016). Briefly, a time step
917 of 20 fs was used, the Verlet cut-off scheme was used considering a buffer tolerance of 0.005 kJ/(mol
918 ps atom). The reaction-field method was used for Coulomb interactions with a cut-off of 11 Å and a
919 relative permittivity of $\varepsilon_r = 15$. For van der Waals' interactions, a cut-off of 11 Å was used. The
920 velocity rescaling thermostat was employed with a reference temperature of T = 310 K, with a
921 coupling constant of $\tau_T = 1$ ps. For the equilibrations, the Berendsen barostat was employed (p = 1
922 bar, $\tau_p = 3$ ps), whereas the production runs were performed with a Parrinello-Rahman barostat (p =
923 1 bar, $\tau_p = 12$ ps). A semi-isotropic pressure coupling was used for all the systems that contained a
924 lipid bilayer. For all systems, an initial round of equilibration with decreasing constraints applied to
925 the protein beads and lipid beads was performed following the protocol provided by CHARMM-GUI
926 Martini maker module.   For the PRLR-TMD-ICD$_{K235-L284}$ simulations, a total of 11 μs of
927 unconstrained MD were performed of which the first microsecond was considered as equilibration
928 and the last 10 μs as production and used for analysis. For the JAK2-FERM-SH2 and the complex
929 between JAK2-FERM-SH2 in solution, 1 μs of unconstrained simulation was performed. In the case
930 of JAK2-FERM-SH2 or the complex between JAK2-FERM-SH2 and PRLR-TMD-ICD$_{K235-L284}$ near
931 a lipid bilayer, an unconstrained run of 5 μs was performed for each system and the complete
932 trajectory considered for analysis.

934 *All-atom molecular dynamics simulations*
935 All-atom MD simulations were performed using GROMACS 2016 and 2018 (Abraham et al., 2015),
936 using the CHARMM36m force field (Huang et al., 2017) for proteins and the TIP3P model for water.
937 The initial system was minimized followed by position restrained simulation in two different phases,
938 NVT and NPT. A 150 ns run of unconstrained NPT equilibration was then performed. The Berendsen
939 thermostat was used for the constrained relaxation runs and the Nose-Hoover thermostat for the
940 production runs. In all cases, the temperature was 310 K. For the NPT simulations, the Berendsen
941 barostat was used during relaxations and the Parinello-Rahman barostat used in unconstrained
942 production runs. In all cases the target pressure was 1 atm. In all the simulations, the Verlet-cutoff
943 scheme was used with a 2 fs timestep. A cutoff of 12 Å with a switching function starting at 10 Å was
944 used for non-bonded interactions along with periodic boundary conditions. The Particle Mesh Ewald
945 method was used to compute long-range electrostatic forces. Hydrogen atoms were constrained using
946 the LINCS (Hess et al., 1997) algorithm.

948 *Trajectory analyses*
949 Analysis of the obtained trajectories was performed using VMD plugins, GROMACS analysis tools
950 and in-house prepared tcl and python scripts, available on github (see below). For the characterization
951 of the orientation of the JAK2-FERM-SH2+PRLR-ICD$_{K235-E284}$ complex with respect to the lipid

27

952 bilayer we used the geographical coordinate system with latitude and longitude devised by Herzog et
953 al. (Herzog et al., 2017). Lipid densities were calculated with the Volmap plugin from VMD
954 considering only the PO4 beads and a 1Å grid. Density plots are shown as an enrichment score with
955 values representing the percentage of enrichment or depletion with respect to the average value on
956 the system as done previously in (Corradi et al., 2018). All molecular renderings were done with
957 VMD (Humphrey et al., 1996). Protein-protein contact maps were calculated using CONAN
958 (Mercadante et al., 2018).
959

Acknowledgements

965

Additional information

Funding

976

Author contributions

978 **Raul Araya-Secchi**, Formal analysis, Validation, Investigation, Visualization, Methodology,
979 Writing - original draft; **Katrine Bugge**, Formal analysis, Validation, Investigation, Visualization,
980 Methodology, Writing - review and editing; **Pernille Seiffert,** Investigation, Visualization,
981 Methodology, Writing - original draft, Writing - review and editing; **Amalie Petry**, Investigation;
982 **Gitte W. Haxholm,** Investigation, **Kresten Lindorff-Larsen**, Validation, Supervision, Writing -
983 review and editing, Funding; **Stine F. Pedersen**, Conceptualization, Resources, Formal analysis,
984 Supervision, Funding acquisition, Writing - review and editing;; **Lise Arleth,** Conceptualization,
985 Writing - review and editing; Resources, Formal analysis, Supervision, Funding acquisition; **Birthe**
986 **B. Kragelund**, Conceptualization, Formal analysis, Validation, Resources, Formal analysis,
987 Visualization, Supervision, Funding acquisition analysis, Writing - original draft, Writing - review
988 and editing;
989

Author ORCIDs

991 Raul Araya-Secchi https://orcid.org/0000-0002-4872-3553
992 Katrine Bugge https://orcid.org/0000-0002-6286-6243
993 Pernille Seiffert https://orcid.org/0000-0003-4213-5336

994   Amalie Petry

995   Gitte W. Haxholm

996   Kresten Lindorff-Larsen https://orcid.org/0000-0002-4750-6039

997   Stine Falsig Pedersen https://orcid.org/0000-0002-3044-7714

998   Lise Arleth https://orcid.org/0000-0002-4694-4299

999   Birthe B. Kragelund https://orcid.org/0000-0002-7454-1761

1000

Additional files

1002

Supplementary files
1004   MDAR checklist

1005

Data availability
1007 All data needed to evaluate the conclusions in the paper are present in the paper and/or the Supplementary Materials. The MD data and models together with the scripts used in the trajectory analysis are available on Github at https://github.com/Niels-Bohr-Institute-XNS-StructBiophys/PRLRmodel. NMR chemical shifts for the PRLR-ICD$_{G236-Q396}$ are deposited in the BioMagResBank under the accession number 51695.

1012

REFERENCES

1014

Abraham MJ, Murtola T, Schulz R, Páll S, Smith JC, Hess B, Lindahl E. 2015. GROMACS: High performance molecular simulations through multi-level parallelism from laptops to supercomputers. *SoftwareX* **1–2**:19–25. doi:10.1016/j.softx.2015.06.001

Aksamitiene E, Achanta S, Kolch W, Kholodenko BN, Hoek JB, Kiyatkin A. 2011. Prolactin-stimulated activation of ERK1 / 2 mitogen-activated protein kinases is controlled by PI3-kinase / Rac / PAK signaling pathway in breast cancer cells. *Cell Signal* **23**:1794–1805. doi:10.1016/j.cellsig.2011.06.014

Ashkenazy H, Abadi S, Martz E, Chay O, Mayrose I, Pupko T, Ben-Tal N. 2016. ConSurf 2016: an improved methodology to estimate and visualize evolutionary conservation in macromolecules. *Nucleic Acids Res* **44**:W344-50. doi:10.1093/nar/gkw408

Bachelot A, Binart N. 2007. Reproductive role of prolactin. *Reproduction* **133**:361–369. doi:10.1530/REP-06-0299

Basak S, Saikia N, Kwun D, Choi UB, Ding F, Bowen ME. 2022. Different Forms of Disorder in NMDA-Sensitive Glutamate Receptor Cytoplasmic Domains Are Associated with Differences in Condensate Formation. *Biomolecules* **13**. doi:10.3390/BIOM13010004

Bocharov E V., Lesovoy DM, Bocharova O V., Urban AS, Pavlov K V., Volynsky PE, Efremov RG, Arseniev AS. 2018. Structural basis of the signal transduction via transmembrane domain of the human growth hormone receptor. *Biochimica et Biophysica Acta (BBA) - General Subjects* **1862**:1410–1420. doi:10.1016/j.bbagen.2018.03.022

Bole-Feysot C, Goffin V, Edery M, Binart N, Kelly PA. 1998. Prolactin (PRL) and its receptor: actionm signal transduction pathways and phenotypes observed in PRL receptor knockout mice. *Endocr Rev* **19**:225–268.

Bompard G, Martin M, Roy C, Vignon F, Freiss G. 2003. Membrane targeting of protein tyrosine phosphatase PTPL1 through its FERM domain via binding to phosphatidylinositol 4,5-biphosphate. *J Cell Sci* **116**:2519–30. doi:10.1242/jcs.00448

Boutin JM, Jolicoeur C, Okamura H, Gagnon J, Edery M, Shirota M, Banville D, Dusanter-Fourt I, Djiane J, Kelly PA. 1988. Cloning and expression of the rat prolactin receptor, a member of the growth hormone/prolactin receptor gene family. *Cell* **53**:69–77. doi:10.1016/0092-8674(88)90488-6

Brooks AJ, Dai W, O'Mara ML, Abankwa D, Chhabra Y, Pelekanos R a, Gardon O, Tunny K a, Blucher KM, Morton CJ, Parker MW, Sierecki E, Gambin Y, Gomez G a, Alexandrov K, Wilson I a, Doxastakis M, Mark AE, Waters MJ. 2014. Mechanism of Activation of Protein Kinase JAK2 by the Growth Hormone Receptor. *Science (1979)* **344**:1249783–1249783. doi:10.1126/science.1249783

Brooks AJ, Dehkhoda F, Kragelund BB. 2016. Cytokine Receptors. *Principles of Endocrinology and Hormone Action*. doi:10.1007/978-3-319-27318-1

Broutin I, Jomain J-B, Tallet E, van Agthoven J, Raynal B, Hoos S, Kragelund BB, Kelly P a, Ducruix A, England P, Goffin V. 2010. Crystal structure of an affinity-matured prolactin complexed to its dimerized receptor reveals the topology of hormone binding site 2. *J Biol Chem* **285**:8422–33. doi:10.1074/jbc.M109.089128

Brown RJ, Adams JJ, Pelekanos RA, Wan Y, McKinstry WJ, Palethorpe K, Seeber RM, Monks TA, Eidne KA, Parker MW, Waters MJ. 2005. Model for growth hormone receptor activation based on subunit rotation within a receptor dimer. *Nat Struct Mol Biol* **12**:814–821. doi:10.1038/nsmb977

Bugge K, Papaleo E, Haxholm GW, Hopper JTS, Robinson C v, Olsen JG, Lindorff-Larsen K, Kragelund BB. 2016. A combined computational and structural model of the full-length human prolactin receptor. *Nat Commun* **7**:11578. doi:10.1038/ncomms11578

Bugge K, Steinocher H, Brooks AJ, Lindor K, Kragelund BB. 2015. Exploiting Hydrophobicity for Efficient Production of Transmembrane Helices for Structure Determination by NMR Spectroscopy. *Anal Chem* **87**:9126–9131. doi:10.1021/acs.analchem.5b02365

Campbell GS, Argetsinger LS, Ihle JN, Kelly PA, Rillema JA, Carter-Su C. 1994. Activation of JAK2 tyrosine kinase by prolactin receptors in Nb2 cells and mouse mammary gland explants. *Proceedings of the National Academy of Sciences* **91**:5232–5236. doi:10.1073/pnas.91.12.5232

Carracedo A, Pandolfi PP. 2008. The PTEN–PI3K pathway: of feedbacks and cross-talks. *Oncogene* **27**:5527–5541. doi:10.1038/onc.2008.247

Chavent M, Karia D, Kalli AC, Domański J, Duncan AL, Hedger G, Stansfeld PJ, Seiradake E, Jones EY, Sansom MSP. 2018. Interactions of the EphA2 Kinase Domain with PIPs in Membranes: Implications for Receptor Function. *Structure* **26**:1025-1034.e2. doi:10.1016/J.STR.2018.05.003

Chhabra Y, Seiffert P, Gormal RS, Vullings M, Lee CMM, Wallis TP, Dehkhoda F, Indrakumar S, Jacobsen NL, Lindorff-Larsen K, Durisic N, Waters MJ, Meunier FA, Kragelund BB, Brooks A. 2022. Tyrosine Kinases Compete for Growth Hormone Receptor Binding and Regulate Receptor Mobility and Degradation. *SSRN Electronic Journal*. doi:10.2139/ssrn.4260495

Clevenger C v, Rui H. 2022. Breast Cancer and Prolactin – New Mechanisms and Models. *Endocrinology* **163**. doi:10.1210/endocr/bqac122

Corradi V, Mendez-Villuendas E, Ingólfsson HI, Gu R-X, Siuda I, Melo MN, Moussatova A, DeGagné LJ, Sejdiu BI, Singh G, Wassenaar TA, Delgado Magnero K, Marrink SJ, Tieleman DP. 2018. Lipid–Protein Interactions Are Unique Fingerprints for Membrane Proteins. *ACS Cent Sci* **4**:709–717. doi:10.1021/acscentsci.8b00143

1084 Dadhich R, Kapoor S. 2022. Lipidomic and Membrane Mechanical Signatures in Triple-Negative
1085   Breast Cancer: Scope for Membrane-Based Theranostics. *Mol Cell Biochem*.
1086   doi:10.1007/s11010-022-04459-4
1087 de Jong DH, Baoukina S, Ingólfsson HI, Marrink SJ. 2016. Martini straight: Boosting performance
1088   using a shorter cutoff and GPUs. *Comput Phys Commun* **199**:1–7.
1089   doi:10.1016/j.cpc.2015.09.014
1090 de Jong DH, Singh G, Bennett WFD, Arnarez C, Wassenaar TA, Schäfer L V., Periole X, Tieleman
1091   DP, Marrink SJ. 2013. Improved Parameters for the Martini Coarse-Grained Protein Force
1092   Field. *J Chem Theory Comput* **9**:687–697. doi:10.1021/ct300646g
1093 de Vos AM, Ultsch M, Kossiakoff AA. 1992. Human growth hormone and extracellular domain of
1094   its receptor: crystal structure of the complex. *Science* **255**:306–12.
1095 Delaglio F, Grzesiek S, Vuister GW, Zhu G, Pfeifer J, Bax A. 1995. NMRPipe: a multidimensional
1096   spectral processing system based on UNIX pipes. *J Biomol NMR* **6**:277–93.
1097 Delaglio Frank, Grzesiek S, Vuister GW, Zhu G, Pfeifer J, Bax A. 1995. NMRPipe: A
1098   multidimensional spectral processing system based on UNIX pipes. *J Biomol NMR* **6**:277–293.
1099   doi:10.1007/BF00197809
1100 Feng J, Mertz B. 2015. Novel phosphotidylinositol 4,5-bisphosphate binding sites on focal adhesion
1101   kinase. *PLoS One* **10**:1–12. doi:10.1371/journal.pone.0132833
1102 Ferrao RD, Wallweber HJA, Lupardus PJ. 2018. Receptor-mediated dimerization of JAK2 FERM
1103   domains is required for JAK2 activation. *Elife* **7**:1–21.
1104 Gadd SL, Clevenger C v. 2006. Ligand-independent dimerization of the human prolactin receptor
1105   isoforms: functional implications. *Mol Endocrinol* **20**:2734–2746. doi:10.1210/me.2006-0114
1106 Glassman CR, Tsutsumi N, Saxton RA, Lupardus PJ, Jude KM, Christopher Garcia K. 2022.
1107   Structure of a Janus kinase cytokine receptor complex reveals the basis for dimeric activation.
1108   *Science* **376**. doi:10.1126/SCIENCE.ABN8933
1109 Goñi GM, Epifano C, Boskovic J, Camacho-Artacho M, Zhou J, Bronowska A, Martín MT, Eck
1110   MJ, Kremer L, Gräter F, Gervasio FL, Perez-Moreno M, Lietha D. 2014. Phosphatidylinositol
1111   4,5-bisphosphate triggers activation of focal adhesion kinase by inducing clustering and
1112   conformational changes. *Proc Natl Acad Sci U S A* **111**:E3177-86.
1113   doi:10.1073/pnas.1317022111
1114 Goretzki B, Weidemann C, McCray B, Schäfer SL, Jansen J, Tebbe F, Mitrovic S-A, Nöth J,
1115   Donahue JK, Jeffries CM, Steinchen W, Stengel F, Sumner CJ, Hummer G, Hellmich UA.
1116   2023. Crosstalk between regulatory elements in the disordered TRPV4 N-terminus modulates
1117   lipid-dependent channel activity. *bioRxiv*. doi:10.1101/2022.12.21.521430
1118 Hamada K, Shimizu T, Matsui T, Tsukita S, Hakoshima T. 2000. Structural basis of the membrane-
1119   targeting and unmasking mechanisms of the radixin FERM domain. *EMBO J* **19**:4449–62.
1120   doi:10.1093/emboj/19.17.4449
1121 Hannan FM, Elajnaf T, Vandenberg LN, Kennedy SH, Thakker R v. 2022. Hormonal regulation of
1122   mammary gland development and lactation. *Nat Rev Endocrinol*. doi:10.1038/s41574-022-
1123   00742-y
1124 Haxholm GW, Nikolajsen LF, Olsen JG, Fredsted J, Larsen FH, Goffin V, Pedersen SF, Brooks AJ,
1125   Waters MJ, Kragelund BB. 2015. Intrinsically disordered cytoplasmic domains of two
1126   cytokine receptors mediate conserved interactions with membranes. *Biochem J* **468**:495–506.
1127   doi:10.1042/BJ20141243
1128 Hedger G, Sansom MSP, Koldsø H. 2015a. The juxtamembrane regions of human receptor tyrosine
1129   kinases exhibit conserved interaction sites with anionic lipids. *Sci Rep* **5**:9198.
1130   doi:10.1038/srep09198

31

1131 Hedger G, Sansom MSP, Koldsø H. 2015b. The juxtamembrane regions of human receptor tyrosine
1132   kinases exhibit conserved interaction sites with anionic lipids. *Sci Rep* **5**:9198.
1133   doi:10.1038/srep09198
1134 Herzog FA, Braun L, Schoen I, Vogel V. 2017. Structural Insights How PIP2 Imposes Preferred
1135   Binding Orientations of FAK at Lipid Membranes. *J Phys Chem B* **121**:3523–3535.
1136   doi:10.1021/acs.jpcb.6b09349
1137 Hess B, Bekker H, Berendsen HJC, Fraaije JGEM. 1997. LINCS: A linear constraint solver for
1138   molecular simulations. *J Comput Chem* **18**:1463–1472. doi:10.1002/(SICI)1096-
1139   987X(199709)18:12<1463::AID-JCC4>3.0.CO;2-H
1140 Huang J, Rauscher S, Nawrocki G, Ran T, Feig M, de Groot BL, Grubmüller H, MacKerell AD.
1141   2017. CHARMM36m: an improved force field for folded and intrinsically disordered proteins.
1142   *Nat Methods* **14**:71–73. doi:10.1038/nmeth.4067
1143 Huang LJ shen, Constantinescu SN, Lodish HF. 2001. The N-terminal domain of Janus kinase 2 is
1144   required for Golgi processing and cell surface expression of erythropoietin receptor. *Mol Cell*
1145   **8**:1327–1338. doi:10.1016/S1097-2765(01)00401-4
1146 Humphrey W, Dalke A, Schulten K. 1996. VMD: Visual molecular dynamics. *J Mol Graph* **14**:33–
1147   38. doi:10.1016/0263-7855(96)00018-5
1148 Jo S, Cheng X, Islam SM, Huang L, Rui H, Zhu A, Lee HS, Qi Y, Han W, Vanommeslaeghe K,
1149   MacKerell AD, Roux B, Im W. 2014. CHARMM-GUI PDB Manipulator for Advanced
1150   Modeling and Simulations of Proteins Containing Nonstandard Residues. pp. 235–265.
1151   doi:10.1016/bs.apcsb.2014.06.002
1152 Jo S, Kim T, Iyer VG, Im W. 2008. CHARMM-GUI: A web-based graphical user interface for
1153   CHARMM. *J Comput Chem* **29**:1859–1865. doi:10.1002/jcc.20945
1154 Jumper J, Evans R, Pritzel A, Green T, Figurnov M, Ronneberger O, Tunyasuvunakool K, Bates R,
1155   Žídek A, Potapenko A, Bridgland A, Meyer C, Kohl SAA, Ballard AJ, Cowie A, Romera-
1156   Paredes B, Nikolov S, Jain R, Adler J, Back T, Petersen S, Reiman D, Clancy E, Zielinski M,
1157   Steinegger M, Pacholska M, Berghammer T, Bodenstein S, Silver D, Vinyals O, Senior AW,
1158   Kavukcuoglu K, Kohli P, Hassabis D. 2021. Highly accurate protein structure prediction with
1159   AlphaFold. *Nature* **596**:583–589. doi:10.1038/s41586-021-03819-2
1160 Kassem N, Araya-Secchi R, Bugge K, Barclay A, Steinocher H, Khondker A, Wang Y, Lenard AJ,
1161   Bürck J, Sahin C, Ulrich AS, Landreh M, Pedersen MC, Rheinstädter MC, Pedersen PA,
1162   Lindorff-Larsen K, Arleth L, Kragelund BB. 2021. Order and disorder—An integrative
1163   structure of the full-length human growth hormone receptor. *Sci Adv* **7**:eabh3805.
1164   doi:10.1126/sciadv.abh3805
1165 Khan HM, Souza PCT, Thallmair S, Barnoud J, De Vries AH, Marrink SJ, Reuter N. 2020.
1166   Capturing Choline-Aromatics Cation-π Interactions in the MARTINI Force Field. *J Chem*
1167   *Theory Comput* **16**:2550–2560. doi:10.1021/ACS.JCTC.9B01194
1168 Kjaergaard M, Brander S, Poulsen FM. 2011. Random coil chemical shift for intrinsically
1169   disordered proteins: Effects of temperature and pH. *J Biomol NMR* **49**:139–149.
1170   doi:10.1007/s10858-011-9472-x
1171 Kjaergaard M, Kragelund BB. 2017. Functions of intrinsic disorder in transmembrane proteins.
1172   *Cellular and Molecular Life Sciences* **74**:3205–3224. doi:10.1007/s00018-017-2562-5
1173 Kubatzky KF, Ruan W, Gurezka R, Cohen J, Ketteler R, Watowich SS, Neumann D, Langosch D,
1174   Klingmüller U. 2001. Self assembly of the transmembrane domain promotes signal
1175   transduction through the erythropoietin receptor. *Current Biology* **11**:110–115.
1176   doi:10.1016/S0960-9822(01)00018-5

1177 Landau M, Mayrose I, Rosenberg Y, Glaser F, Martz E, Pupko T, Ben-Tal N. 2005. ConSurf 2005:
1178   the projection of evolutionary conservation scores of residues on protein structures. *Nucleic*
1179   *Acids Res* **33**:W299-302. doi:10.1093/nar/gki370

1180 Larsen AH, John LH, Sansom MSP, Corey RA. 2022. Specific interactions of peripheral membrane
1181   proteins with lipids: what can molecular simulations show us? *Biosci Rep* **42**.
1182   doi:10.1042/BSR20211406

1183 Larsen AH, Wang Y, Bottaro S, Grudinin S, Arleth L, Lindorff-Larsen K. 2020. Combining
1184   molecular dynamics simulations with small-angle X-ray and neutron scattering data to study
1185   multi-domain proteins in solution. *PLoS Comput Biol* **16**:e1007870.
1186   doi:10.1371/journal.pcbi.1007870

1187 Lee J, Cheng X, Swails JM, Yeom MS, Eastman PK, Lemkul JA, Wei S, Buckner J, Jeong JC, Qi
1188   Y, Jo S, Pande VS, Case DA, Brooks CL, MacKerell AD, Klauda JB, Im W. 2016.
1189   CHARMM-GUI Input Generator for NAMD, GROMACS, AMBER, OpenMM, and
1190   CHARMM/OpenMM Simulations Using the CHARMM36 Additive Force Field. *J Chem*
1191   *Theory Comput* **12**:405–413. doi:10.1021/acs.jctc.5b00935

1192 Lu J, Dong W, Hammond GR, Hong Y. 2022. Hypoxia controls plasma membrane targeting of
1193   polarity proteins by dynamic turnover of PI4P and PI(4,5)P2. *Elife* **11**.
1194   doi:10.7554/eLife.79582

1195 Maeda R, Sato T, Okamoto K, Yanagawa M, Sako Y. 2018. Lipid-Protein Interplay in Dimerization
1196   of Juxtamembrane Domains of Epidermal Growth Factor Receptor. *Biophys J* **114**:893–903.
1197   doi:10.1016/j.bpj.2017.12.029

1198 Mani T, Hennigan RF, Foster LA, Conrady DG, Herr AB, Ip W. 2011. FERM Domain
1199   Phosphoinositide Binding Targets Merlin to the Membrane and Is Essential for Its Growth-
1200   Suppressive Function. *Mol Cell Biol* **31**:1983–1996. doi:10.1128/MCB.00609-10

1201 Mayzel M, Rosenlo J, Orekhov VY. 2014. Time-resolved multidimensional NMR with non-
1202   uniform sampling. *J Biomol NMR* **58**:129–139. doi:10.1007/s10858-013-9811-1

1203 McLaughlin S, Smith SO, Hayman MJ, Murray D. 2005. An Electrostatic Engine Model for
1204   Autoinhibition and Activation of the Epidermal Growth Factor Receptor (EGFR/ErbB)
1205   Family. *Journal of General Physiology* **126**:41–53. doi:10.1085/jgp.200509274

1206 McLaughlin S, Wang J, Gambhir A, Murray D. 2002. PIP(2) and proteins: interactions,
1207   organization, and information flow. *Annu Rev Biophys Biomol Struct* **31**:151–75.
1208   doi:10.1146/annurev.biophys.31.082901.134259

1209 McNally R, Toms A V., Eck MJ. 2016. Crystal Structure of the FERM-SH2 Module of Human
1210   Jak2. *PLoS One* **11**:e0156218. doi:10.1371/journal.pone.0156218

1211 Mercadante D, Gräter F, Daday C. 2018. CONAN: A Tool to Decode Dynamical Information from
1212   Molecular Interaction Maps. *Biophys J* **114**:1267–1273. doi:10.1016/j.bpj.2018.01.033

1213 Metcalf DG, Moore DT, Wu Y, Kielec JM, Molnar K, Valentine KG, Wand AJ, Bennett JS,
1214   DeGrado WF. 2010. NMR analysis of the αIIbβ3 cytoplasmic interaction suggests a
1215   mechanism for integrin regulation. *Proceedings of the National Academy of Sciences*
1216   **107**:22481–22486. doi:10.1073/pnas.1015545107

1217 Morris R, Kershaw NJ, Babon JJ. 2018. The molecular details of cytokine signaling via the
1218   JAK/STAT pathway. *Protein Science* **27**:1984–2009. doi:10.1002/pro.3519

1219 Newey PJ, Gorvin CM, Cleland SJ, Willberg CB, Bridge M, Azharuddin M, Drummond RS, van
1220   der Merwe PA, Klenerman P, Bountra C, Thakker R v. 2013. Mutant Prolactin Receptor and
1221   Familial Hyperprolactinemia. *New England Journal of Medicine* **369**:2012–2020.
1222   doi:10.1056/NEJMoa1307557

1223 Orekhov VY, Jaravine VA. 2011. Analysis of non-uniformly sampled spectra with multi-
1224   dimensional decomposition. *Prog Nucl Magn Reson Spectrosc* **59**:271–292.
1225   doi:10.1016/j.pnmrs.2011.02.002
1226 Park MJ, Sheng R, Silkov A, Jung DJ, Wang ZG, Xin Y, Kim H, Thiagarajan-Rosenkranz P, Song
1227   S, Yoon Y, Nam W, Kim I, Kim E, Lee DG, Chen Y, Singaram I, Wang L, Jang MH, Hwang
1228   CS, Honig B, Ryu S, Lorieau J, Kim YM, Cho W. 2016. SH2 Domains Serve as Lipid-Binding
1229   Modules for pTyr-Signaling Proteins. *Mol Cell* **62**. doi:10.1016/j.molcel.2016.01.027
1230 Patwardhan P, Resh MD. 2010. Myristoylation and membrane binding regulate c-Src stability and
1231   kinase activity. *Mol Cell Biol* **30**:4094–4107. doi:10.1128/MCB.00246-10
1232 Pettersen EF, Goddard TD, Huang CC, Couch GS, Greenblatt DM, Meng EC, Ferrin TE. 2004.
1233   UCSF Chimera - A visualization system for exploratory research and analysis. *J Comput Chem*
1234   **25**:1605–1612. doi:10.1002/jcc.20084
1235 Pezet A, Buteau H, Kelly PA, Edery M. 1997. The last proline of Box 1 is essential for association
1236   with JAK2 and functional activation of the prolactin receptor. *Mol Cell Endocrinol* **129**:199–
1237   208. doi:10.1016/S0303-7207(97)00063-4
1238 Qi Y, Ingólfsson HI, Cheng X, Lee J, Marrink SJ, Im W. 2015. CHARMM-GUI Martini Maker for
1239   Coarse-Grained Simulations with the Martini Force Field. *J Chem Theory Comput* **11**:4486–
1240   4494. doi:10.1021/acs.jctc.5b00513
1241 Rawat A, Harishchandran A, Nagaraj R. 2013. Fatty acyl chain-dependent but charge-independent
1242   association of the SH4 domain of Lck with lipid membranes. *J Biosci* **38**:63–71.
1243   doi:10.1007/s12038-012-9288-1
1244 Rawat A, Nagaraj R. 2010. Determinants of membrane association in the SH4 domain of Fyn: roles
1245   of N-terminus myristoylation and side-chain thioacylation. *Biochim Biophys Acta* **1798**:1854–
1246   63. doi:10.1016/j.bbamem.2010.06.009
1247 Roberts E, Eargle J, Wright D, Luthey-Schulten Z. 2006. MultiSeq: unifying sequence and structure
1248   data for evolutionary analysis. *BMC Bioinformatics* **7**:382. doi:10.1186/1471-2105-7-382
1249 Rowlinson SW, Yoshizato H, Barclay JL, Brooks AJ, Behncken SN, Kerr LM, Millard K,
1250   Palethorpe K, Nielsen K, Clyde-Smith J, Hancock JF, Waters MJ. 2008. An agonist-induced
1251   conformational change in the growth hormone receptor determines the choice of signalling
1252   pathway. *Nat Cell Biol* **10**:740–7. doi:10.1038/ncb1737
1253 Rui H, Kirken RA, Farrar WL. 1994. Activation of receptor-associated tyrosine kinase JAK2 by
1254   prolactin. *J Biol Chem* **269**:5364–8.
1255 Russell RB, Barton GJ. 1992. Multiple protein sequence alignment from tertiary structure
1256   comparison: Assignment of global and residue confidence levels. *Proteins: Structure,*
1257   *Function, and Genetics* **14**:309–323. doi:10.1002/prot.340140216
1258 Sackmann-Sala L, Goffin V. 2015. Prolactin-Induced Prostate Tumorigenesis. pp. 221–242.
1259   doi:10.1007/978-3-319-12114-7_10
1260 Seiffert P, Bugge K, Nygaard M, Haxholm GW, Martinsen JH, Pedersen MN, Arleth L, Boomsma
1261   W, Kragelund BB. 2020a. Orchestration of signaling by structural disorder in class 1 cytokine
1262   receptors. *Cell Communication and Signaling* **18**. doi:10.1186/s12964-020-00626-6
1263 Seiffert P, Bugge K, Nygaard M, Haxholm GW, Martinsen JH, Pedersen MN, Arleth L, Boomsma
1264   W, Kragelund BB. 2020b. Orchestration of signaling by structural disorder in class 1 cytokine
1265   receptors. *Cell Communication and Signaling* **18**. doi:10.1186/s12964-020-00626-6
1266 Seubert N, Royer Y, Staerk J, Kubatzky KF, Moucadel V, Krishnakumar S, Smith SO,
1267   Constantinescu SN. 2003. Active and Inactive Orientations of the Transmembrane and
1268   Cytosolic Domains of the Erythropoietin Receptor Dimer. *Mol Cell* **12**:1239–1250.
1269 Shen M-Y, Sali A. 2006. Statistical potential for assessment and prediction of protein structures.
1270   *Protein Sci* **15**:2507–24. doi:10.1110/ps.062416606

1271   Sheng R, Jung DJ, Silkov A, Kim H, Singaram I, Wang ZG, Xin Y, Kim E, Park MJ, Thiagarajan-
1272   Rosenkranz P, Smrt S, Honig B, Baek K, Ryu S, Lorieau J, Kim YM, Cho W. 2016. Lipids
1273   regulate Lck protein activity through their interactions with the Lck Src homology 2 domain.
1274   *Journal of Biological Chemistry* **291**:17639–17650. doi:10.1074/jbc.M116.720284
1275   Souza PCT, Marrink SJS. 2020. Martini 3 - Open Beta-Release. *http://cgmartini.nl*.
1276   Stefanski KM, Russell CM, Westerfield JM, Lamichhane R, Barrera FN. 2021. PIP2promotes
1277   conformation-specific dimerization of the EphA2 membrane region. *Journal of Biological*
1278   *Chemistry* **296**. doi:10.1074/jbc.RA120.016423
1279   Suh BC, Hille B. 2005. Regulation of ion channels by phosphatidylinositol 4,5-bisphosphate. *Curr*
1280   *Opin Neurobiol* **15**:370–378. doi:10.1016/J.CONB.2005.05.005
1281   Thomasen FE, Pesce F, Roesgaard MA, Tesei G, Lindorff-Larsen K. 2022. Improving Martini 3 for
1282   Disordered and Multidomain Proteins. *J Chem Theory Comput* **18**:2033–2041.
1283   doi:10.1021/acs.jctc.1c01042
1284   Trimble WS, Grinstein S. 2015. Barriers to the free diffusion of proteins and lipids in the plasma
1285   membrane. *Journal of Cell Biology* **208**:259–271. doi:10.1083/jcb.201410071
1286   van den Bogaart G, Meyenberg K, Risselada HJ, Amin H, Willig KI, Hubrich BE, Dier M, Hell
1287   SW, Grubmüller H, Diederichsen U, Jahn R. 2011. Membrane protein sequestering by ionic
1288   protein–lipid interactions. *Nature* **479**:552–555. doi:10.1038/nature10545
1289   Varadi M, Anyango S, Deshpande M, Nair S, Natassia C, Yordanova G, Yuan D, Stroe O, Wood G,
1290   Laydon A, Žídek A, Green T, Tunyasuvunakool K, Petersen S, Jumper J, Clancy E, Green R,
1291   Vora A, Lutfi M, Figurnov M, Cowie A, Hobbs N, Kohli P, Kleywegt G, Birney E, Hassabis
1292   D, Velankar S. 2022. AlphaFold Protein Structure Database: massively expanding the
1293   structural coverage of protein-sequence space with high-accuracy models. *Nucleic Acids Res*
1294   **50**:D439–D444. doi:10.1093/nar/gkab1061
1295   Vranken WF, Boucher W, Stevens TJ, Fogh RH, Pajon A, Llinas M, Ulrich EL, Markley JL,
1296   Ionides J, Laue ED. 2005. The CCPN data model for NMR spectroscopy: Development of a
1297   software pipeline. *Proteins: Structure, Function, and Bioinformatics* **59**:687–696.
1298   doi:10.1002/prot.20449
1299   Wallweber HJA, Tam C, Franke Y, Starovasnik MA, Lupardus PJ. 2014. Structural basis of
1300   recognition of interferon-α receptor by tyrosine kinase 2. *Nat Struct Mol Biol* **21**:443–448.
1301   doi:10.1038/nsmb.2807
1302   Webb B, Sali A. 2016. Comparative Protein Structure Modeling Using MODELLER. *Curr Protoc*
1303   *Bioinformatics* **54**. doi:10.1002/cpbi.3
1304   Wilmes S, Hafer M, Vuorio J, Tucker JA, Winkelmann H, Löchte S, Stanly TA, Pulgar Prieto KD,
1305   Poojari C, Sharma V, Richter CP, Kurre R, Hubbard SR, Garcia KC, Moraga I, Vattulainen I,
1306   Hitchcock IS, Piehler J. 2020. Mechanism of homodimeric cytokine receptor activation and
1307   dysregulation by oncogenic mutations. *Science (1979)* **367**:643–652.
1308   doi:10.1126/science.aaw3242
1309   Yamauchi T, Kaburagi Y, Ueki K, Tsuji Y, Stark GR, Kerr IM, Tsushima T, Akanuma Y, Komuro
1310   I, Tobe K, Yazaki Y, Kadowaki T. 1998. Growth Hormone and Prolactin Stimulate Tyrosine
1311   Phosphorylation of Insulin Receptor Substrate-1, -2, and -3, Their Association with p85
1312   Phosphatidylinositol 3-Kinase (PI3-kinase), and Concomitantly PI3-kinase Activation via
1313   JAK2 Kinase. *Journal of Biological Chemistry* **273**:15719–15726.
1314   doi:10.1074/jbc.273.25.15719
1315   Zhang D, Wlodawer A, Lubkowski J. 2016. Crystal Structure of a Complex of the Intracellular
1316   Domain of Interferon λ Receptor 1 (IFNLR1) and the FERM/SH2 Domains of Human JAK1. *J*
1317   *Mol Biol* **428**:4651–4668. doi:10.1016/j.jmb.2016.10.005
1318

1319

1320 **FIGURE LEGENDS**

1321 **Fig. 1: Schematics of the PRLR:PRL:JAK2 complex in the membrane.** The PRLR is shown in
1322 light blue, the PRL as a dark blue triangle, the PRLR-ICD as a disordered chain and JAK2 in purple.
1323 The PI(4,5)P$_2$ lipid (PIP2) is shown in orange. The intracellular juxtamembrane (ICJM) region and
1324 BOX1 of PRLR-ICD are highlighted in green nuances, while the three LIDs as defined in Haxholm
1325 et al., (Haxholm et al., 2015) are highlighted in red. For simplicity only one of the two ICDs is shown
1326 associated with JAK2 via the BOX1 (green) and BOX2 (orange) motifs.

1327

1328 **Fig. 2: The ICJM region of the PRLR interacts with PI(4,5)P$_2$. A)** Overview of investigated PRLR
1329 variants. **B)** Secondary chemical shifts (SCSs) of TMD-ICD$_{F206-S270}$ reconstituted in DHPC micelles.
1330 **C)** Correlation plot of the SCSs of ICD$_{G236-Q396}$ plotted against those of TMD-ICD$_{F206-S270}$. **D)** ^{15}N,^{1}H-
1331 HSQC spectra of ^{15}N-ICD$_{K235-G313}$ titrated with 5x, 10x and 25x molar excess of C$_8$-PI(4,5)P$_2$. **E)**
1332 Structure of C$_8$-PI(4,5)P$_2$. **F)** Backbone amide chemical shift perturbations (CSPs) and peak intensity
1333 changes upon addition of C$_8$-PI(4,5)P$_2$ to ^{15}N-ICD$_{K235-G313}$ plotted against residue number. **G) Top**:
1334 Far-UV CD spectra of Pep1 titrated with C$_8$-PI(4,5)P$_2$ or in 65% TFE. **Middle:** Far-UV CD spectra
1335 of Pep1 in the presence of 5x-38x C$_8$-PI(4,5)P$_2$ subtracted with the spectrum of Pep1 in the absence
1336 of C$_8$-PI(4,5)P$_2$. **Bottom**: Far-UV CD spectra of Pep2 titrated with C$_8$-PI(4,5)P$_2$ or in 65% TFE.
1337 **Figure supplement 1**: *^{15}N, ^{1}H-HSQC spectra of A) TMD$_{F206-V240}$ and TMD-ICD$_{F206-S270}$ in DHPC*
1338 *micelles, and (B) TMD-ICD$_{F206-S270}$ in POPC SUVs.*
1339 **Figure supplement 2**: *C$^\alpha$ secondary chemical shifts of ICD$_{G236-Q396}$*

1340

1341 **Fig. 3. Protein – lipid interactions of PRLR-ICD$_{LID1}$ obtained from CG-MD simulations. (A-**
1342 **B)** Protein – lipids contact histograms for PRLR-ICD$_{LID1}$+POPC:POPS:PI(4,5)P$_2$ (80:10:10). **A)**
1343 Contacts between the protein and lipid headgroups. A contact is counted if the distance between the
1344 backbone beads of the protein is ≤ 7 Å from the head-group beads of the lipids. **B)** Contacts between
1345 the protein and the acyl chains of the lipids. A contact is counted if the distance between the backbone
1346 bead of the protein is ≤ 7 Å from the acyl-chain bead of the lipids. **C)** Correlation between the change
1347 in NMR signal and the contact frequency between PRLR-ICD$_{LID1}$ and the lipid headgroups from the
1348 PRLR-ICD$_{LID1}$ + POPC:POPS:PI(4,5)P$_2$ (80:10:10) system. Pearson correlation coefficient of -0.55
1349 with $p = 4.0\text{x}10^{-5}$ and R^2 = 0.3. **D)** Average PI(4,5)P$_2$ density map (*xy*-plane) taken from the PRLR-
1350 ICD$_{LID1}$ + POPC:POPS:PI(4,5)P$_2$ (80:10:10) simulation. The map is colored according to the
1351 enrichment/depletion percentage with respect to the average density value. **E)** Schematic
1352 representation of how the interactions and the embedment into the membrane of PRLR contribute to
1353 the co-structure formation. The data from the simulations correspond to those of the production stage
1354 (see methods).

1355

1356 **Figure supplement 1**: *Protein – lipid interactions of PRLR-ICD$_{LID1}$ obtained from CG-MD*
1357 *simulations using the martini 3.0b3.2 forcefield*
1358 **Figure supplement 2**: Complementary analysis of the Protein e Protein – lipid interactions of PRLR-
1359 ICD$_{LID1}$ obtained from CG-MD simulations.

1360

1361 **Fig. 4. Protein – lipid interactions of the JAK2-FERM-SH2 PRLR-ICD$_{LID1}$ complex obtained**
1362 **from CG-MD simulations**. **A)** Schematic representation of the simulated system. Combined **B)**
1363 JAK2-FERM-SH2-lipid and **C)** PRLR-ICD$_{LID1}$-lipid contact frequency histograms for the 16 CG
1364 simulations of the JAK2-FERM-SH2 +PRLR-ICD$_{LID1}$+ POPC:POPS:PI(4,5)P$_2$ system. **D)**
1365 Distribution of the orientations adopted by the JAK2-FERM-SH2 + PRLR-ICD$_{LID1}$ complex when
1366 bound to lipids taken from the 16 simulations with POPC:POPS:PI(4,5)P$_2$ in the lower-leaflet. The
1367 snapshots surrounding the map correspond to representative conformations of the highlighted states
1368 also indicating the fraction total bound time for which each state was observed. Representative
1369 conformations of **E)** State 2 and **F)** State 4. The grey cylinder depicts the position where PRLR-TMD
1370 should be located. Representative protein-lipid contact histograms for **G)** State2 and **H)** State4
1371 colored as in panels B and C.
1372 **Figure supplement 1**: *Analysis of the JAK2-FERM-SH2- PRLR-ICD$_{LID1}$ AA-MD simulation*.
1373 **Figure supplement 2.** *Complementary analysis of Protein – lipid interactions of the JAK2-FERM-*
1374 *SH2 PRLR-ICD$_{LID1}$ complex obtained from CG-MD simulations*
1375 **Figure supplement 3.** *Snapshots of the different binding states observed for the JAK2-FERM-SH2 –*
1376 *PRLR-ICD$_{LID1}$ complex with the complete structural model of JAK2*
1377
1378 **Fig. 5. PRLR variants with mutations in lipid interacting residues exhibit decreased PRL-**
1379 **stimulated STAT5 activation in AP1-2PH-PLCδ-GFP cells. A)** NMR intensity changes of
1380 ICD$_{K235-G313}$ WT, K4G, K4E, φ4G and GAG variants upon titration with 5x, 10x and 25x molar
1381 excess C$_8$-PI(4,5)P$_2$ plotted against residue number. **B)** The PRLR variants (WT, K4G, K4E, φ4G,
1382 3GAG) were transiently transfected in AP1 cells stably expressing the 2PH-PLCδ-GFP construct
1383 which visualizes the plasma membrane by binding PI(4,5)P$_2$. The cells were subsequently analysed
1384 by immunofluorescence microscopy, using antibodies against PRLR (magenta) and GFP (green), as
1385 well as DAPI (blue) to mark nuclei. To the right, examples of an average line-scan for each PRLR
1386 variant is shown. The fluorescence intensity depicted along the white line drawn (arrow) and green
1387 fluorescence (plasma membrane) was used to divide the line in a plasma membrane section and
1388 intracellular section, and relative membrane localization was calculated as the average fluorescence
1389 of PRLR in the membrane section divided by that in the intracellular section. **C, D)** AP1-2PH-PLCδ-
1390 GFP cells were transiently transfected with PRLR variants (WT, K4G, K4E, φ4G, 3GAG, K2E$_{253}$,
1391 K2E$_{261}$) and incubated overnight followed by serum starvation for 16-17 h and were subsequently
1392 incubated with or without 10 nM prolactin for 30 min. The resulting lysates were analysed by western
1393 blot for STAT5, pSTAT5 (Y964), PRLR, β-actin and p150 levels. The immunoblots are
1394 representative of three biological replicates. **E)** Ratio of plasma membrane localized receptor
1395 compared to intracellular receptor, analysed by line-scans as in B. Each point represents an individual
1396 cell, and data are based on three independent biological experiments per condition. Graphs show
1397 means with SEM error bars. *P<0.05, **P<0.01 and ****P<0.0001. One-way ANOVA compared to
1398 WT, unpaired. **F)** Quantification of western blot results shown as pSTAT5 normalized to total
1399 STAT5, relative to the WT condition. Graphs show means with SEM error bars. *P<0.05 and
1400 **P<0.01. One-way ANOVA compared to WT, unpaired.
1401 **Source file 1**: Raw western blots (relating to *figure 5C*)
1402 **Source file 2**: Raw western blot (relating to *figure 5D*)

1403   **Source file 3**: Data summaries (relating to *figure 5E,F*)

1404   **Figure supplement 1**: *Chemical shift perturbations of ICD$_{K235-G313}$ of A) WT, B) K4E, C) GAG, D)*

1405   *K4G and E) ϕ4G variants.*

1406   **Figure supplement 2:** *^{15}N R_2 relaxation rates of ICD$_{K235-G313}$ of WT (grey bars), K4G (blue dots)*

1407   *and ϕ4G (red squares) variants.*

1408

1409   **Fig. 6. Model of how co-structure formation between JAK2, PRLR and PI4(4,5)P$_2$ may**

1410   **contribute to signalling fidelity.** The suggested states in signalling would be **A**) the inactive state of

1411   the co-structure exemplified by the Flat orientation. **B**) The hormone bound state expemplfied by the

1412   co-structure in the Y orientation. **C**) Phosphorylation of PIP(4,5)P$_2$ to PI(3,4,5)P$_3$ for which the PRLR

1413   has no affinity may lead to downregulation and/or termination of signalling. The colour scheme of

1414   the proteins is identical to Fig.4.

1415

1416   **Figure supplements and Supplementary files**

1417

1418   **The prolactin receptor scaffolds Janus kinase 2 via co-structure**

1419   **formation with phosphoinositide-4,5-bisphosphate**

1420   Raul Araya-Secchi[1,2], Katrine Bugge[3#], Pernille Seiffert[3#], Amalie Petry[4], Gitte W. Haxholm[3],

1421   Kresten Lindorff-Larsen[3], Stine F. Pedersen[4*], Lise Arleth[1*] and Birthe B. Kragelund[3*]

1422

1423   [1]Structural Biophysics, Section for Neutron and X-ray Science, Niels Bohr Institute, University of
1424   Copenhagen, 2100 Copenhagen, Denmark.
1425   [2]Facultad de Ingenieria Arquitectura y Diseño, Universidad San Sebastian, Bellavista 7, Santiago,
1426   Chile.
1427   [3]Structural Biology and NMR Laboratory (SBiNLab), Department of Biology, University of
1428   Copenhagen, 2200 Copenhagen, Denmark.
1429   [4]Section for Cell Biology and Physiology, Department of Biology, University of Copenhagen, 2200
1430   Copenhagen N, Denmark

1431

1432

1433 **Overview of contents:**

1434 **Figure supplements for main figures:**

1449   **Figure 5 – Figure supplement** 2: ^{15}N R_2 relaxation rates of $ICD_{K235-G313}$ of WT (grey bars), K4G (blue dots)

1450   and ϕ4G (red squares) variants.

1451

1452   **Supplementary files not directly related to any main figures:**

1453   **Movie 1**: Y State (STATE 2) from the JAK2-FERM-SH2 PRLR-$ICD_{K235-E284}$ complex simulated near a bilayer

1454   containing $PI(4,5)P_2$: Representative trajectory showing State 2 (Y). Protein and lipids colored as in Fig. 4

1455   **Movie 2**: FLAT State (STATE 4) from the JAK2-FERM-SH2 PRLR-$ICD_{K235-E284}$ complex simulated near a

1456   bilayer containing $PI(4,5)P_2$: Representative trajectory showing State 4 (Y). Protein and lipids colored as in

1457   Fig. 4
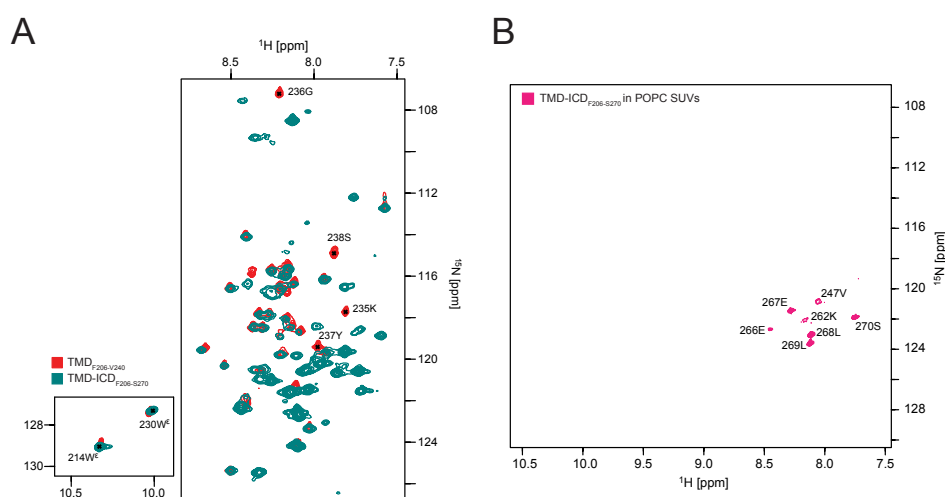
1458

1459   **Figure 2 – figure supplement 1.** ^{15}N, ^{1}H-HSQC spectra of A) $TMD_{F206-V240}$ and TMD-$ICD_{F206-S270}$ in DHPC

1460   micelles, and (B) TMD-$ICD_{F206-S270}$ in POPC SUVs.

1461

1462
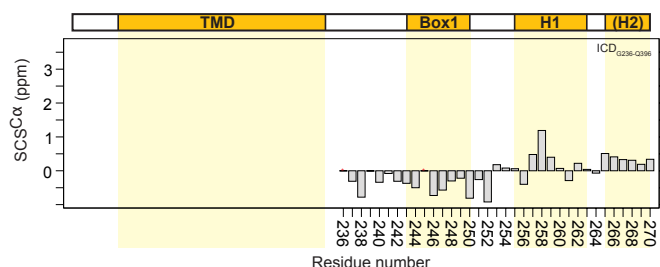
1463

1464   **Figure 2 – figure supplement 2.** C^{α} secondary chemical shifts of $ICD_{G236-Q396}$.
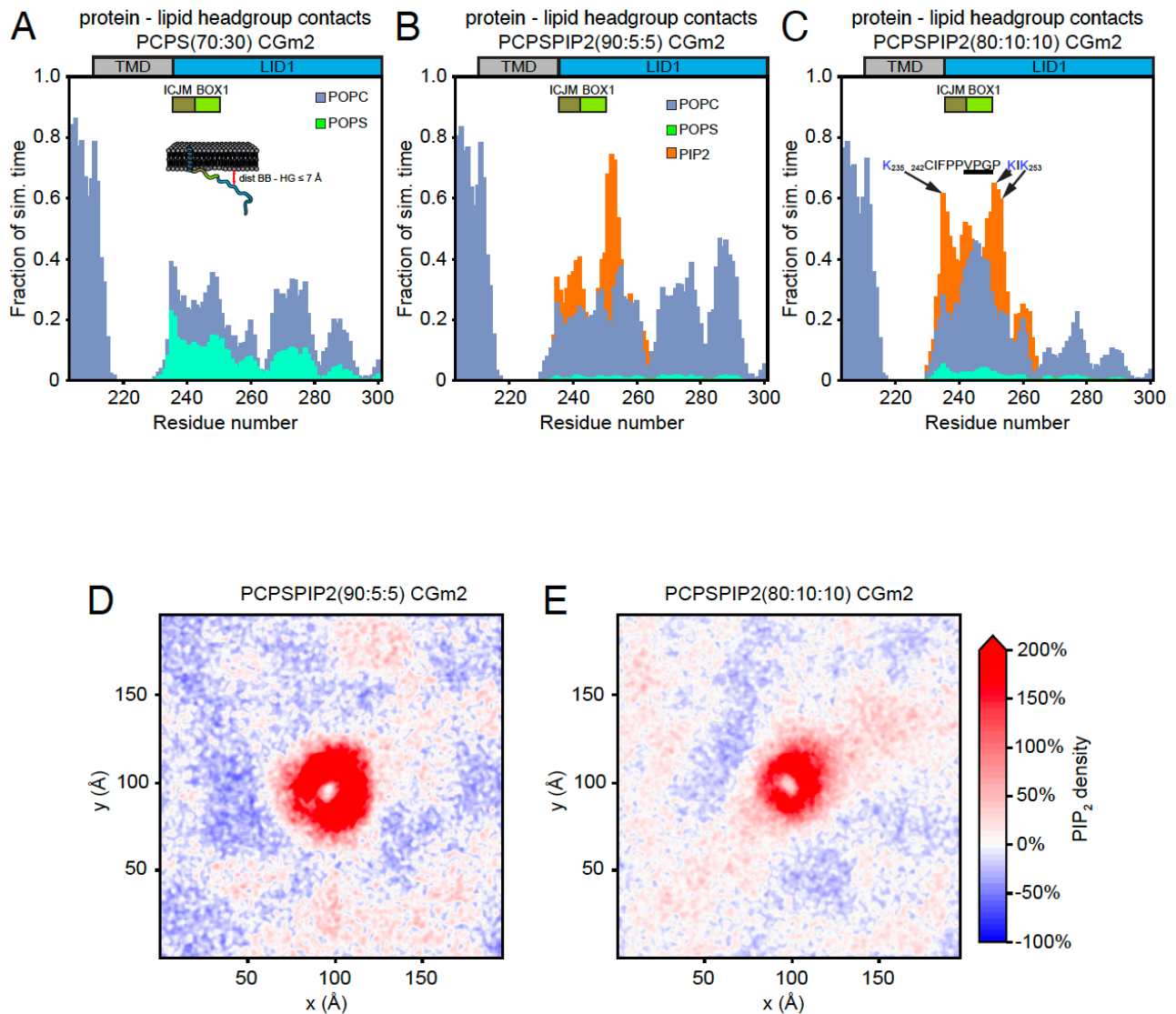
Figure 3 – figure supplement 1. Protein – lipid interactions of PRLR-ICD$_{LID1}$ obtained from CG-MD simulations using the martini 2.2 forcefield. *(A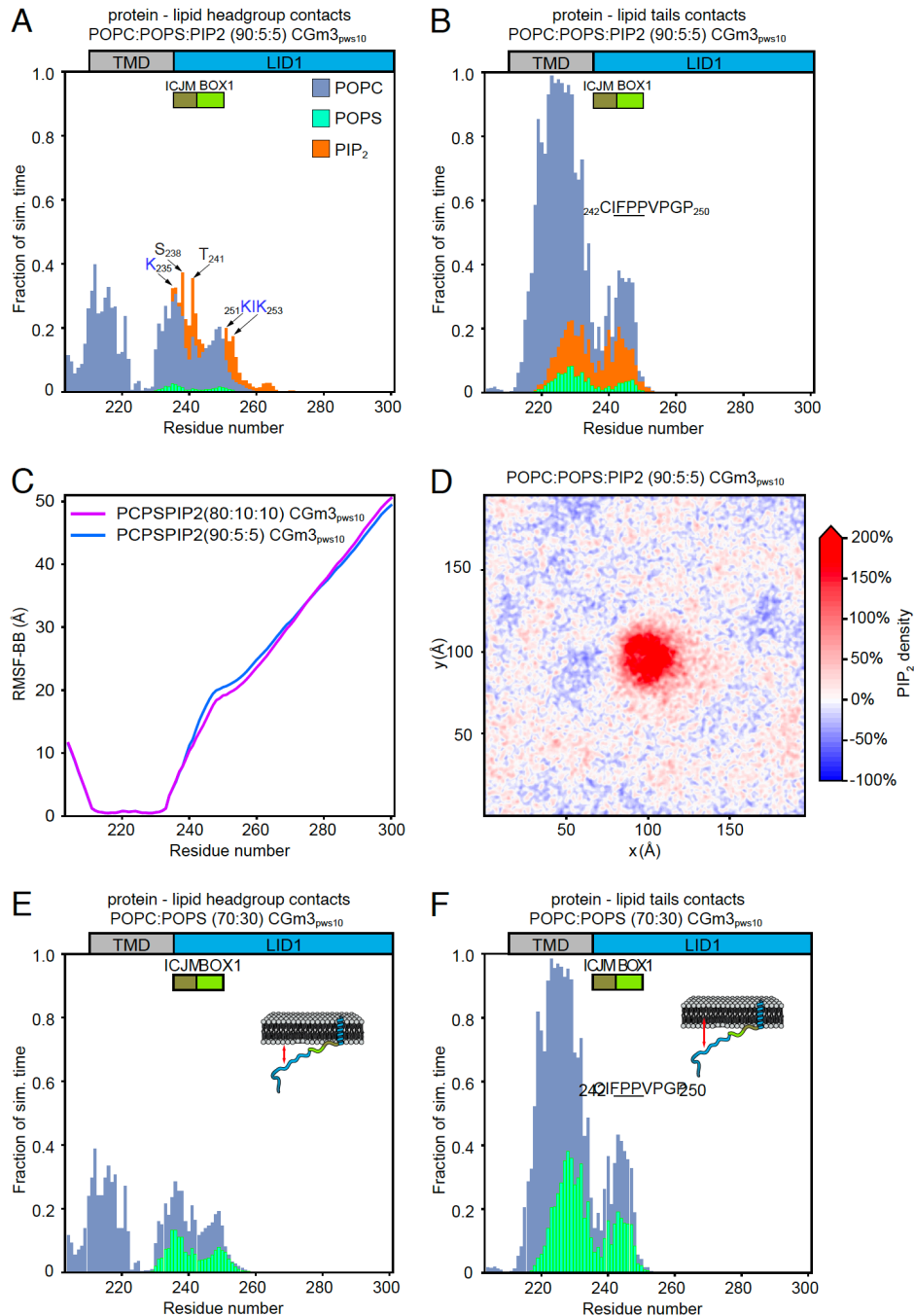-C)* Protein – lipid-headgroups contact histograms from: (A) the PRLR-ICD$_{LID1}$ POPC:POPS (70:30) CGm2 simulation, (B) PRLR-ICD$_{LID1}$ POPC:POPS:PI(4,5)P$_2$ (90:5:5) CGm2 simulation and (C) PRLR-ICD$_{LID1}$ PRLR-ICD$_{LID1}$POPC:POPS:PI(4,5)P$_2$ (80:10:10) CGm2 simulation.
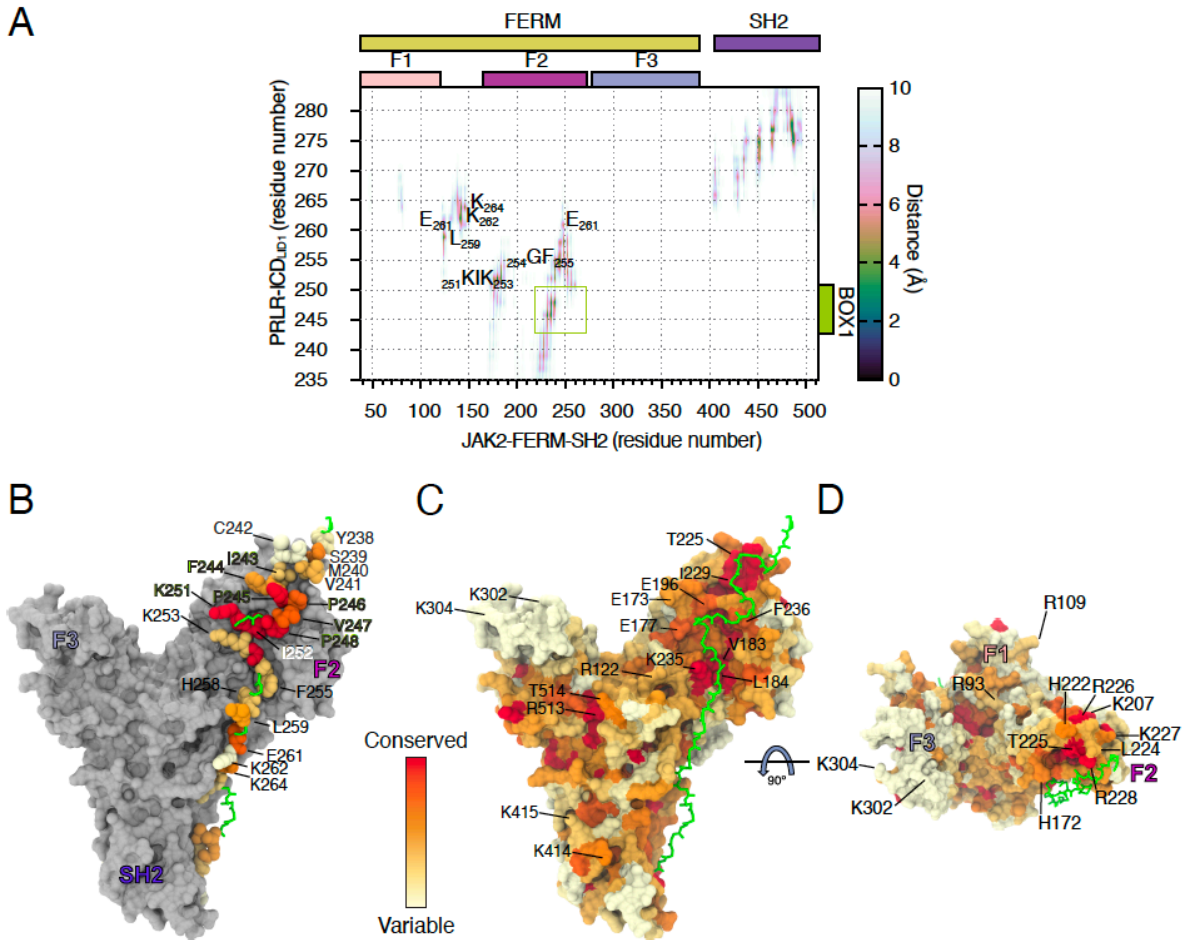
1473

Figure 3 – figure supplement 2: Complementary analysis of protein – lipid interactions of PRLR-ICD$_{LID1}$ obtained from CG-MD simulations using the martini 3.0b3.2 forcefield. (A-B) Protein – lipids contact histograms from the PRLR-ICD$_{LID1}$ POPC:POPS:PI(4,5)P$_2$ (90:5:5) CGm3$_{pws10}$ simulation. (A) Contacts between the protein and lipid headgroups. (B) Contacts between the protein and the acyl chains of the lipids. (C) RMSF of the BB beads obtained from the PRLR-ICD$_{LID1}$POPC:POPS:PI(4,5)P$_2$ (80:10:10) CGm3$_{pws10}$ simulation (Magenta line) and the PRLR-ICD$_{LID1}$ POPC:POPS:PI(4,5)P$_2$ (90:5:5) CGm3$_{pws10}$ simulation (blue line). (D) Average PI(4,5)P$_2$ density map (*xy*-plane) taken from the PRLR-ICD$_{LID1}$ + POPC:POPS:PI(4,5)P$_2$(90:5:5) CGm3$_{pws10}$ simulation. (E-F) Protein – lipids contact histograms from the PRLR-ICD$_{LID1}$ POPC:POPS (30:70) CGm3$_{pws10}$ simulation. (E) Contacts between the protein and lipid headgroups. (F) Contacts between the protein and the acyl chains of the lipids. In A-B and E-F protein – lipid contacts are defined as in Figure 3.

1485

1486

1487

Figure 4 - Figure supplement 1: **Analysis of the JAK2-FERM-SH2- PRLR-ICD$_{K235-H300}$ AA-MD simulation.** A) Average distance map between JAK2-FERM-SH2 and PRLR-ICD$_{K235-H300}$ obtained from the all-atom MD simulation. (B) Conservation of residues from PRLR in contact with JAK2-FERM-SH2 (see A). Residues with green label correspond to BOX1. (C-D) Conservation JAK2-FERM-SH2 oriented as state 2 (see Fig. 4E). Labeled residues correspond to residues that contact PRLR (see A) or that contact the lipids on states 2 and 4 (see Fig. 4E-H).

1488
1489
1490
1491
1492
1493
1494
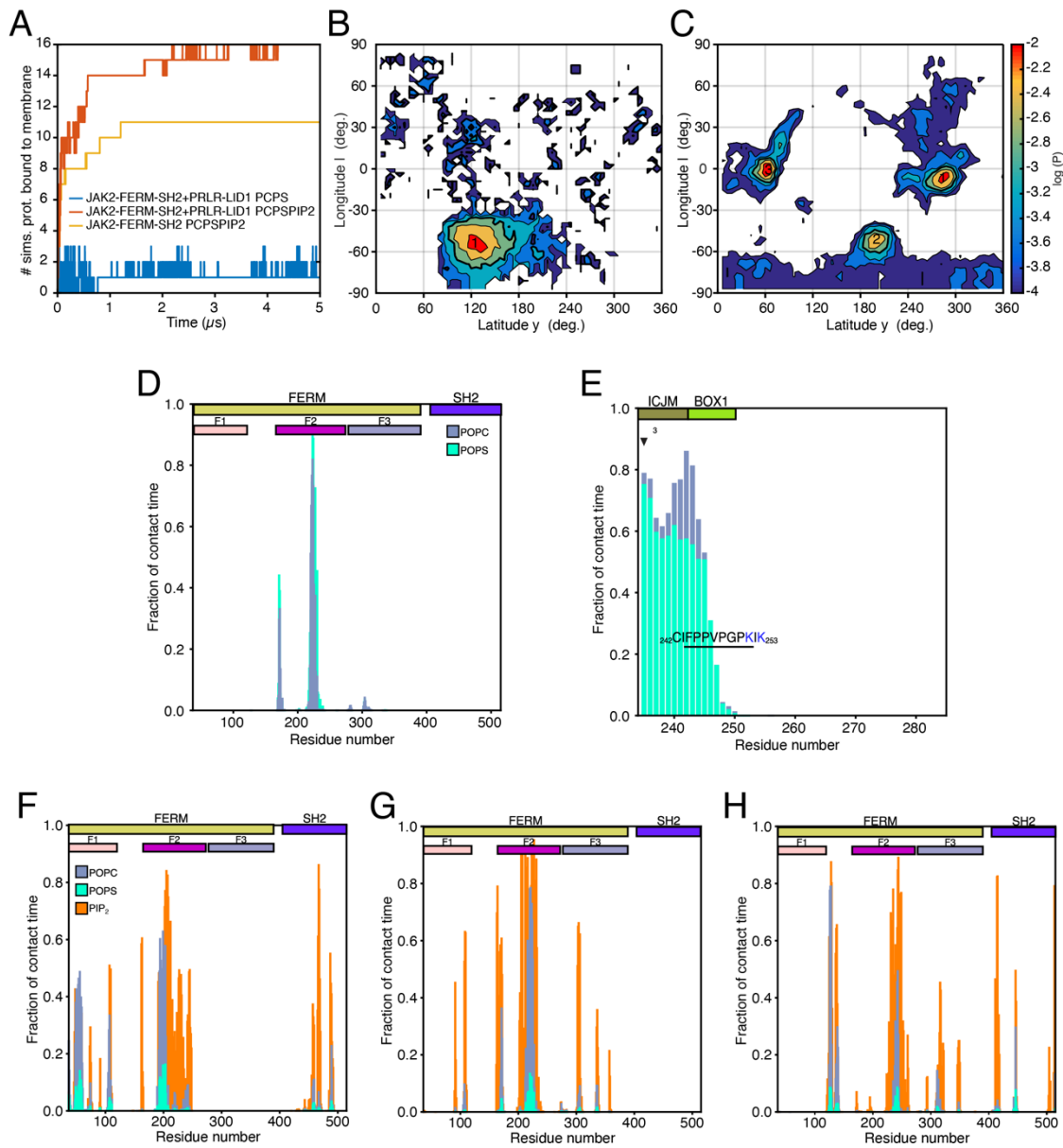
1495

1519

Figure 4 - Figure Supplement 2. Complementary analysis of Protein – lipid interactions of the JAK2-FERM-SH2 PRLR-ICD$_{K235-H300}$ complex obtained from CG-MD simulations (A) Number of simulations where protein is bound to the lower-leaf of the bilayer for the simulations containing: the JAK2-FERM-SH2 + PRLR-ICD$_{K235-H300}$ complex near a POPC:POPS(70:30) bilayer (blue line) and the JAK2-FERM-SH2 + PRLR-ICD$_{K235-H300}$ complex (red line) and the apo JAK2-FERM-SH2 (orange line)near a POPC:POPS:PI(4,5)P$_2$ (80:10:10) bilayer. (B-C) Distribution of the orientations adopted by (B) the JAK2-FERM-SH2 + PRLR-ICD$_{K235-H300}$ complex when bound to lipids taken from the simulations with POPC:POPS(70:30) in the lower-leaflet and (C) the apo JAK2-FERM-SH2 when bound to lipids taken from the simulations with POPC:POPS:PI(4,5)P$_2$ (80:10:10) in the lower-leaflet. (D-E) Representative protein-lipid contact histograms for State 1 observed for the JAK2-FERM-SH2 + PRLR- ICD$_{K235-H300}$ complex near a POPC:POPS(70:30) bilayer. (F-H) Representative protein-lipid contact histograms for States 1, 2 and 3 observed for the apo JAK2-FERM-SH2 near a POPC:POPS:PI(4,5)P$_2$ (80:10:10) bilayer.

44

1532
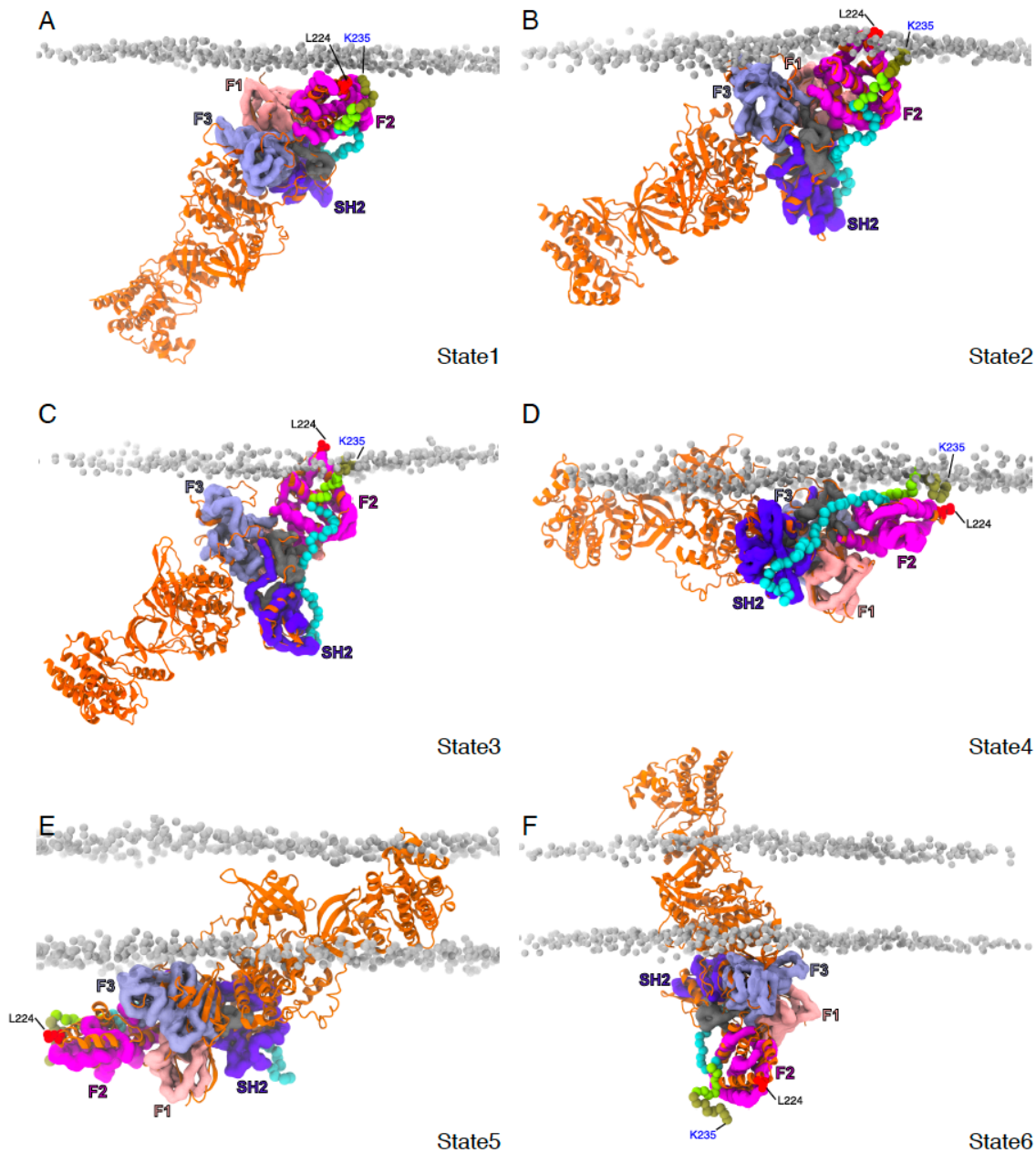
1533

1534

Figure 4 - Figure Supplement 3. Snapshots of the different binding states observed for the JAK2-FERM-SH2 – PRLR-ICD$_{K235-H300}$ complex with the complete structural model of JAK2 (obtained from AF2-EBI database). In each panel the CG JAK2-FERM-SH2 – PRLR-ICD$_{K235-H300}$ complex is depicted and colored as in Fig. 4. The full-length JAK2 model is shown in cartoon representation colored orange. near a POPC:POPS(70:30) bilayer. (F-H) Representative protein-lipid contact histograms for States 1, 2 and 3 observed for the apo JAK2-FERM-SH2 near a POPC:POPS:PI(4,5)P$_2$ (80:10:10) bilayer.

1541

1542

45
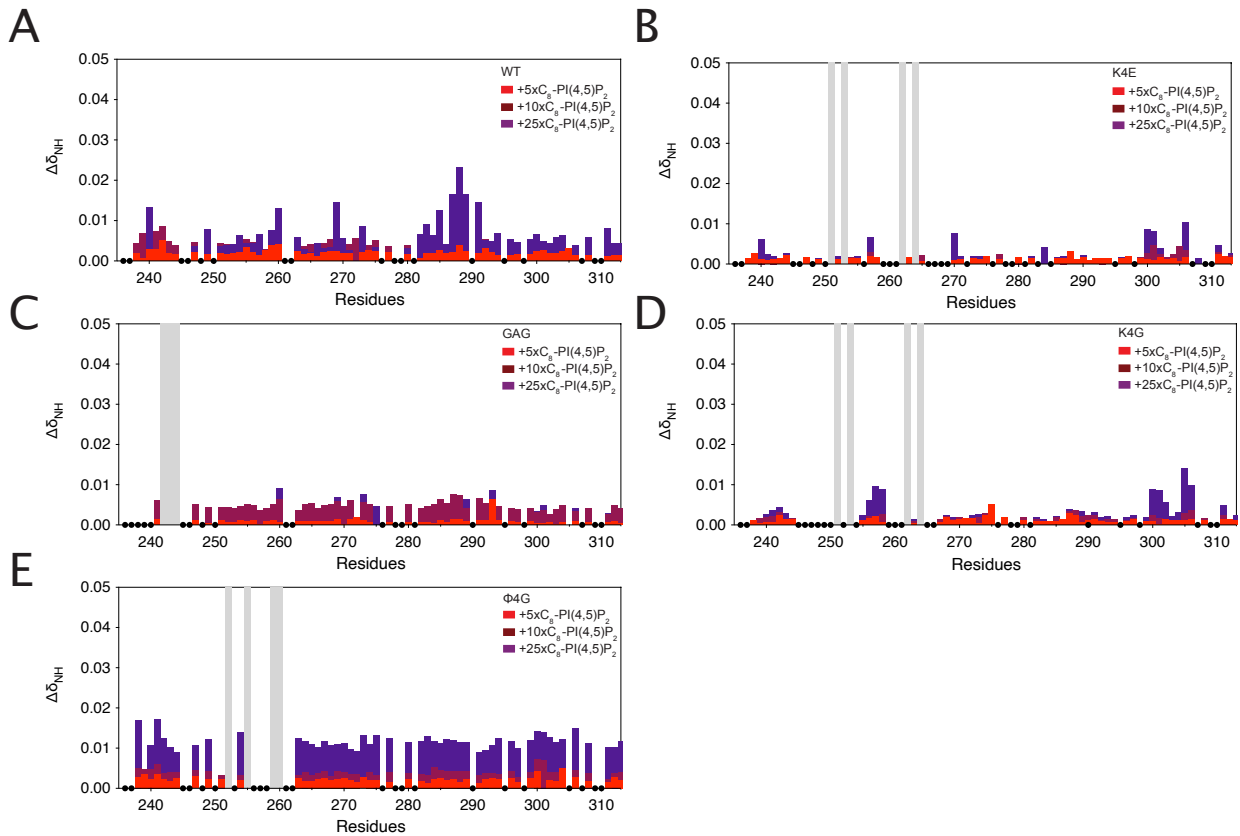
Figure 5 – Figure supplement 1: Chemical shift perturbations of $ICD_{K235-G313}$ of A) WT B) K4E, C) GAG, D) K4G and E) ϕ4G variants.
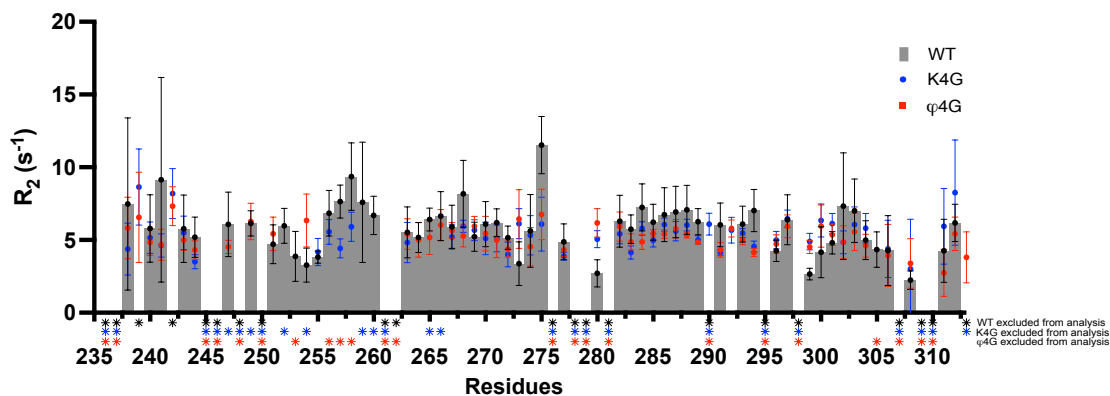
Figure 5 – Figure supplement 2: ^{15}N R_2 relaxation rates of $ICD_{K235-G313}$ of WT (grey bars), K4G (blue dots) and ϕ4G (red squares) variants. Stars indicate signals excluded from the analysis either because it is a proline, signals are overlapping or a poor exponential fit.